Available online at www.sciencedirect.com
SCIENCE DIRECT®
Nuclear Instruments and Methods in Physics Research A 501 (2003) 418–462
NUCLEAR INSTRUMENTS & METHODS IN PHYSICS RESEARCH Section A
www.elsevier.com/locate/nima

The Super-Kamiokande detector

S. Fukuda[a], Y. Fukuda[a], T. Hayakawa[a], E. Ichihara[a], M. Ishitsuka[a], Y. Itow[a], T. Kajita[a], J. Kameda[a], K. Kaneyuki[a], S. Kasuga[a], K. Kobayashi[a], Y. Kobayashi[a], Y. Koshio[a], M. Miura[a], S. Moriyama[a], M. Nakahata[a], S. Nakayama[a], T. Namba[a], Y. Obayashi[a], A. Okada[a], M. Oketa[a], K. Okumura[a], T. Oyabu[a], N. Sakurai[a], M. Shiozawa[a], Y. Suzuki[a], Y. Takeuchi[a], T. Toshito[a], Y. Totsuka[a], S. Yamada[a], S. Desai[a], M. Earl[a], J.T. Hong[b], E. Kearns[b], M. Masuzawa[b,1], M.D. Messier[b,2], J.L. Stone[b,3], L.R. Sulak[b], C.W. Walter[b], W. Wang[b], K. Scholberg[c], T. Barszczak[d], D. Casper[d], D.W. Liu[d], W. Gajewski[d], P.G. Halverson[d,4], J. Hsu[d], W.R. Kropp[d], S. Mine[d], L.R. Price[d], F. Reines[d,✠], M. Smy[d], H.W. Sobel[d], M.R. Vagins[d], K.S. Ganezer[e], W.E. Keig[e], R.W. Ellsworth[f], S. Tasaka[g], J.W. Flanagan[h,1], A. Kibayashi[h], J.G. Learned[h], S. Matsuno[h], V.J. Stenger[h], Y. Hayato[i], T. Ishii[j], A. Ichikawa[j], J. Kanzaki[j], T. Kobayashi[j], T. Maruyama[j,5], K. Nakamura[j], Y. Oyama[j], A. Sakai[j], M. Sakuda[j], O. Sasaki[j], S. Echigo[k], T. Iwashita[k], M. Kohama[k], A.T. Suzuki[k], M. Hasegawa[l], T. Inagaki[l], I. Kato[l], H. Maesaka[l], T. Nakaya[l], K. Nishikawa[l], S. Yamamoto[l], T.J. Haines[m,d], B.K. Kim[n], R. Sanford[n], R. Svoboda[n], E. Blaufuss[o], M.L. Chen[o], Z. Conner[o,6], J.A. Goodman[o], E. Guillian[o], G.W. Sullivan[o], D. Turcan[o], A. Habig[p], M. Ackerman[q], F. Goebel[q], J. Hill[q,6], C.K. Jung[q], T. Kato[q], D. Kerr[q], M. Malek[q], K. Martens[q,1], C. Mauger[q], C. McGrew[q], E. Sharkey[q], B. Viren[q,7], C. Yanagisawa[q,*], W. Doki[r], S. Inaba[r], K. Ito[r], M. Kirisawa[r], M. Kitaguchi[r], C. Mitsuda[r], K. Miyano[r], C. Saji[r], M. Takahata[r], M. Takahashi[r], K. Higuchi[s], Y. Kajiyama[s], A. Kusano[s], Y. Nagashima[s], K. Nitta[s], M. Takita[s], T. Yamaguchi[s], M. Yoshida[s,8], H.I. Kim[t], S.B. Kim[t], J. Yoo[t], H. Okazawa[u], M. Etoh[v],

*Corresponding author. Tel.: +1-631-632-8105; fax: +1-631-632-8101.
E-mail address: chiaki@superk.physics.sunysb.edu (C. Yanagisawa).
[1] Present address: Accelerator Laboratory, High Energy Accelerator Research Organization (KEK), Japan.
[2] Present address: Department of Physics, Indiana University, Bloomington, IN 47405, USA.
[3] Present address: Institute of Particle and Nuclear Studies, High Energy Accelerator Research Organization (KEK), Japan.
[4] Present address: NASA, JPL, Pasadena, CA 91109, USA.
✠ Deceased.
[5] Present address: Enrico Fermi Institute, University of Chicago, Chicago, IL 60637, USA.
[6] Present address: Department of Physics, California State University, Dominguez Hills, Carson, CA 90747, USA.
[7] Present address: Phyisics Department, Brookhaven National Laboratory, Upton, NY 11973, USA.
[8] Present address: Accelerator Laboratory, High Energy Accelerator Research Organization (KEK), Japan.

0168-9002/03/$ - see front matter
doi:10.1016/S0168-9002(03)00425-X

K. Fujita[v], Y. Gando[v], A. Hasegawa[v], T. Hasegawa[v], S. Hatakeyama[v], K. Inoue[v], K. Ishihara[v], T. Iwamoto[v], M. Koga[v], I. Nishiyama[v,✠], H. Ogawa[v], J. Shirai[v], A. Suzuki[v], T. Takayama[v], F. Tsushima[v], M. Koshiba[w], Y. Ichikawa[x], T. Hashimoto[x], Y. Hatakeyama[x], M. Koike[x], T. Horiuchi[x], M. Nemoto[x], K. Nishijima[x], H. Takeda[x], H. Fujiyasu[i], T. Futagami[i], H. Ishino[i], Y. Kanaya[i], M. Morii[i], H. Nishihama[i], H. Nishimura[i], T. Suzuki[i], Y. Watanabe[i], D. Kielczewska[y,d], U. Golebiewska[y], H.G. Berns[z], S.B. Boyd[z,9], R.A. Doyle[z], J.S. George[z,10], A.L. Stachyra[z,11], L.L. Wai[z,12], R.J. Wilkes[z], K.K. Young[z,✠], H. Kobayashi[aa]

[a] *Institute for Cosmic Ray Research, University of Tokyo, 5-1-5 Kashiwa-no-Ha, Kashiwa, Chiba 277-8582, Japan*
[b] *Department of Physics, Boston University, Boston, MA 02215, USA*
[c] *Department of Physics, Massachusetts Institute of Technology, Cambridge, MA 02139, USA*
[d] *Department of Physics and Astronomy, University of California, Irvine, Irvine, CA 92697-4575, USA*
[e] *Department of Physics, California State University, Dominguez Hills, Carson, CA 90747, USA*
[f] *Department of Physics, George Mason University, Fairfax, VA 22030, USA*
[g] *Department of Physics, Gifu University, Gifu, Gifu 501-1193, Japan*
[h] *Department of Physics and Astronomy, University of Hawaii, Honolulu, HI 96822, USA*
[i] *Department of Physics, Tokyo Institute for Technology, Meguro, Tokyo 152-8551, Japan*
[j] *Institute of Particle and Nuclear Studies, High Energy Accelerator Research Organization (KEK), Tsukuba, Ibaraki 305-0801, Japan*
[k] *Department of Physics, Kobe University, Kobe, Hyogo 657-8501, Japan*
[l] *Department of Physics, Kyoto University, Kitashirakawa, Kyoto 606-8502, Japan*
[m] *Los Alamos National Laboratory, Physics Division, P-23, Los Alamos, NM 87544, USA*
[n] *Department of Physics and Astronomy, Louisiana State University, Baton Rouge, LA 70803, USA*
[o] *Department of Physics, University of Maryland, College Park, MD 20742, USA*
[p] *Department of Physics, University of Minnesota, Duluth, Duluth, MN 55812-3009, USA*
[q] *Department of Physics and Astronomy, State University of New York at Stony Brook, Stony Brook, NY 11794-3800, USA*
[r] *Department of Physics, Niigata University, Niigata, Niigata 950-2181, Japan*
[s] *Department of Physics, Osaka University, Toyonaka, Osaka 560-0043, Japan*
[t] *Department of Physics, Seoul National University, Seoul 151-742, South Korea*
[u] *International and Cultural Studies, Shizuoka Seiko College, Yaizu, Shizuoka 425-8611, Japan*
[v] *Department of Physics, Tohoku University, Sendai, Miyagi 980-8578, Japan*
[w] *The University of Tokyo, Tokyo 113-0033, Japan*
[x] *Department of Physics, Tokai University, Hiratsuka, Kanagawa 259-1292, Japan*
[y] *Institute of Experimental Physics, Warsaw University, 00-681 Warsaw, Poland*
[z] *Department of Physics, University of Washington, Seattle, WA 98195-1560, USA*
[aa] *Acclerator Laboratory, High Energy Accelerator Research Organization (KEK), Tsukuba, Ibaraki 305-0801, Japan*

The Super-Kamiokande Collaboration

Received 11 December 2002; accepted 9 January 2003

Abstract

Super-Kamiokande is the world's largest water Cherenkov detector, with net mass 50,000 tons. During the period April, 1996 to July, 2001, Super-Kamiokande I collected 1678 live-days of data, observing neutrinos from the Sun,

[9] Present address: University of Pittsburgh, Pittsburgh, PA 15260, USA.
[10] Present address: California Institute of Technology, Pasadena, CA 91125, USA.
[11] Present address: MIT Lincoln Labs, Lexington, MA 02420, USA.
[12] Present address: Department of Physics, Stanford University, CA 94305, USA.

Earth's atmosphere, and the K2K long-baseline neutrino beam with high efficiency. These data provided crucial information for our current understanding of neutrino oscillations, as well as setting stringent limits on nucleon decay. In this paper, we describe the detector in detail, including its site, configuration, data acquisition equipment, online and offline software, and calibration systems which were used during Super-Kamiokande I.

PACS: 29.40.K; 96.40.T; 14.60.P; 96.60.J

Keywords: Water Cherenkov detector; Super-Kamiokande; Neutrinos; K2K; Cosmic rays

1. Introduction

Super-Kamiokande is the world's largest water Cherenkov detector. Located in Kamioka Township, Gifu Prefecture, Japan, the detector is operated by the Super-Kamiokande Collaboration, a joint Japan–US research collaboration, using facilities provided by the Kamioka Observatory of the Institute of Cosmic Ray Research (ICRR), University of Tokyo.

The scientific goals of the Super-Kamiokande experiment include searches for proton decays, and studies of neutrinos from various sources: the Sun, atmosphere, supernovae, gamma ray bursters, and other astrophysical sources, as well as artificial neutrino beams. Previous publications describe significant Super-Kamiokande results, including the first unambiguous evidence of neutrino oscillation in atmospheric neutrinos [1]; confirmation of the solar neutrino flux deficit and with realtime observations proof that solar neutrinos really come from the Sun [2]; first measurement of the solar neutrino energy spectrum above 5 MeV [3]; the world's highest lower limits on partial lifetimes for nucleon decay modes such as $p \to e^+\pi^0$ and $p \to \nu K^+$ [4,5].

Super-Kamiokande was commissioned and data taking began in April, 1996. It was shut down for maintenance and upgrade in July, 2001, after logging 1678 live days of running with high efficiency. In this paper we will describe the detector hardware, triggering, software (for both realtime data acquisition (DAQ) and offline data reduction and archiving), and calibration procedures, as configured for this initial 1996–2001 running period, referred to as Super-Kamiokande I. During refilling operations in preparation for Super-Kamiokande II, in November, 2001, an apparent cascade of implosions triggered by a single photomultiplier (PMT) implosion destroyed over half of the PMTs in the detector [6]. Work in progress at the time of writing is expected to result in re-commissioning of the detector by the end of 2002, with temporarily reduced PMT coverage (47% of Super-Kamiokande I). The configuration and operational characteristics of the rebuilt detector and its associated software will be described later, in a separate publication. In this paper, use of the present tense indicates detector features and components which are expected to continue to be present (perhaps upgraded) with Super-Kamiokande II.

In the next section, we will provide an overview of the detector and its operation, define frequently used terms and acronyms, and summarize the most commonly needed statistics, facts and figures. Subsequent sections will provide details of detector subsystems, and DAQ, reduction and analysis procedures.

2. Overview

Super-Kamiokande is located in the Mozumi mine of the Kamioka Mining and Smelting Company, near the village of Higashi–Mozumi, Gifu, Japan. The detector cavity lies under the peak of Mt. Ikenoyama, with 1000 m of rock, or 2700 m-water-equivalent (m.w.e.) mean overburden, at geographic coordinates 36°25′32.6″N, 137°18′37.1″E, and altitude 370 m above the conventional (WGS-84) geodetic ellipsoid, as determined by a GPS survey [7]. The location of Super-Kamiokande is indicated by a black dot in

Fig. 1. Location of Super-Kamiokande in Japan.

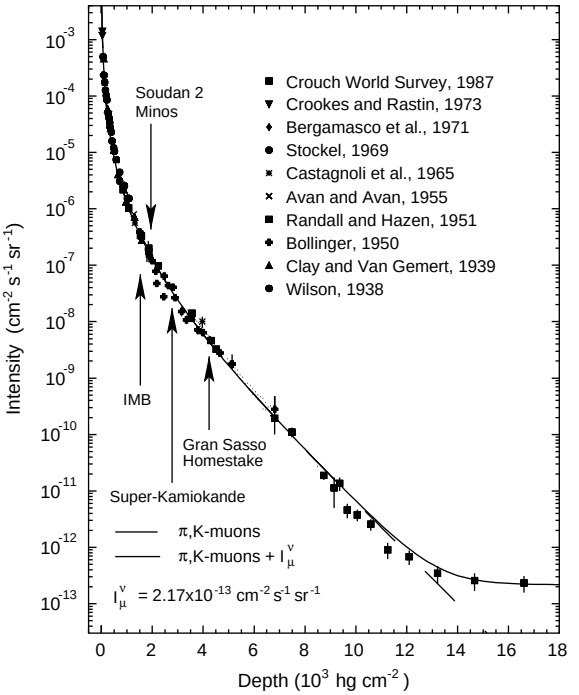

Fig. 2. Cosmic ray muon flux as a function of depth in 10^3 hg cm^{-2} equivalent to km w.e. together with the depths of present and past underground experiments [8].

Fig. 1. Access to the detector site is through a 1.8 km long, nominally horizontal mine tunnel, wide enough for large trucks, with secondary access via a mine railway.

Cosmic ray muons with energy of less than 1.3 TeV cannot penetrate to a depth of 2700 m.w.e. The observed muon flux, which does not pose a significant background for the experiment, is 6×10^{-8} cm^{-2} s^{-1} sr^{-1}. Muon flux as a function of depth for past and current underground experiments, including Super-Kamiokande, is shown in Fig. 2 [8].

The measured rates for other possible backgrounds in the mine near the Super-Kamiokande cavity are given in Table 1 [9].

The Super-Kamiokande water Cherenkov detector consists of a welded stainless-steel tank, 39 m diameter and 42 m tall, with total nominal water capacity of 50,000 tons. Access to the tank is through a set of 2 hatches on the tank top, in addition to a hatch providing access to the tank bottom. All hatches are pressure-sealed to isolate the environment within the tank from light leaks and ambient radioactivity. The tank top itself is used as a platform to support electronics huts, equipment for calibrations, water quality monitoring, and other facilities.

Table 1
Measured background radiation rates for γ rays and neutrons near the Kamiokande cavity dome [9]

Particle	Energy range	Rate
γ rays	$E_\gamma > 0.5$ MeV	0.1 cm^{-2} s^{-1} sr^{-1}
	$E_\gamma > 5$ MeV	2.7×10^{-6} cm^{-2} s^{-1} sr^{-1}
Neutrons	$E_n \leqslant 5 \times 10^{-2}$ eV	1.4×10^{-5} cm^{-2} s^{-1}
	$5 \times 10^{-2} < E_n \leqslant 2.5 \times 10^6$ eV	2.5×10^{-5} cm^{-2} s^{-1}
	$2.5 \times 10^6 < E_n \leqslant 2.5 \times 10^7$ eV	0.33×10^{-5} cm^{-2} s^{-1}

Within the tank, a stainless-steel framework of thickness 55 cm, spaced approximately 2–2.5 m inside the tank walls on all sides, supports separate arrays of inward-facing (at about 2.5 m inside the wall) and outward-facing (at about 2 m inside the wall) PMTs. The inward-facing array consists of 11,146 Hamamatsu Type R3600 50 cm diameter hemispherical PMTs. The inward-facing PMTs,

and the volume of water they view, are referred to as the Inner Detector (ID). The density of PMTs in the ID was such that effectively 40% of the ID surface area was covered by photocathode.

Optically isolated from the ID is an array of 1885 outward-facing Hamamatsu R1408 20 cm diameter hemispherical PMTs. These PMTs, and the water volume they view, are referred to as the Outer Detector (OD). The OD is lined with reflective Tyvek® material manufactured by DuPont, and each OD PMT is attached to a $50\,\text{cm} \times 50\,\text{cm}$ acrylic wavelength shifting (WS) plate. These features improve light collection efficiency for the OD, compensating for the relatively sparse PMT array. Section 4 provides a detailed description of the tank, ID and OD.

Super-Kamiokande can detect events over a wide range of energy, from 4.5 MeV to over 1 TeV. Each ID PMT has a dynamic range from 1 photoelectron (pe) to 300 pe. For low energy events used for solar neutrino studies, the energy of the event is calculated from the number of PMT hits, while for high energy events used in atmospheric neutrino and muon studies the energy is measured in terms of net charge detected by PMTs.

Neutrino interactions are detected via the Cherenkov light emitted by the charged particles produced. Events due to entering charged particles can be identified using the OD PMTs. Neutrino interaction candidates produced in the ID are defined as events producing Cherenkov light in the ID equivalent to deposition of about 4.5 MeV or more, with no evidence of entering particles in the OD. Details of triggers and preprocessing of event data will be given in Section 5. Here, we will simply define the terminology used for various event categories, for later reference.

Neutrino events produced in the ID are termed "fully contained" (FC) if there is no activity in the OD indicating exiting or entering particles. The size, shape, and orientation of the Cherenkov light pattern produced on the ID walls can be used to identify the event as single-ring electron-like (e-like), single-ring muon-like (μ-like), or multi-ring. Events with OD light patterns consistent with exiting particles are termed "partially contained" (PC). For these events, the energy deposited in the detector is only a lower limit on the neutrino energy.

Upward going muons which are assumed to be products of neutrino interactions in the rock below Super-Kamiokande, are also recorded. For upward muons, Cherenkov light patterns consistent with an entering muon are required. If OD data show that the particle also exits the detector, it is termed a "through-going upward muon"; if not, it is a "stopping upward muon". Finally, downward going muons, products of meson decay in the atmosphere, are observed at a net rate of about 2 Hz. These events provide useful housekeeping and calibration data.

Each PMT is connected to high voltage supplies and signal processing electronics via a single cable. These cables are all brought up to the tank top, where they are distributed to four "quadrant-huts" which contain electronics racks and front-end DAQ computers serving ID and OD PMTs for one quadrant of the detector.

Signals from ID PMTs are sent to custom-designed ATM (Analog-Timing-Modules) which provide arrival time and pulse area information with effectively no deadtime, due to a 2-channel ping–pong DAQ technique: when an ATM channel is busy, subsequent signals are sent to the alternate channel for processing. Details of the ID DAQ are given in Section 5.2.

Characteristics of the OD PMTs differed sufficiently from those of the ID PMTs that an independent DAQ was required. OD PMT cables are similarly routed to the appropriate quadrant-hut, where signals are processed by custom-designed QTC (charge-to-time converters) which output digital pulses with length proportional to the input pulse area. QTC signals are sent to pipeline Time-to-Digital Converters (TDCs), which digitize the time of each leading and trailing edge. Details of the OD DAQ are given in Section 5.3.

Another electronics hut, the "Central Hut", contains electronics and associated computers for triggering, housekeeping, and Global Positioning System (GPS) time synchronization systems. These systems are described in detail in Section 5.

To maximize water transparency and minimize backgrounds due to natural radioactivity, the

water used to fill the Cherenkov detector tank is highly purified by a multi-step system including filtration, reverse osmosis (RO) and degasification. Water purity is maintained by recirculation through the purification system. In addition, to mitigate the relatively high radon background present in the mine, the tank area is supplied with fresh air pumped in from a site outside and well away from the mine entrance. These systems are described in detail in Sections 7.1 and 7.2.

Just outside the mine entrance, a prefabricated hut was built to house the dome air system (see Section 7.2). The "Radon Hut" is also used to house the dual GPS antennae and receivers used for precise absolute time synchronization (see Section 5.5). The GPS receivers are linked to the DAQ in the central hut via a 2 km long dual optical fiber cable, allowing each trigger to be time-stamped with 60 ns precision.

A large variety of calibration procedures are used in the Super-Kamiokande experiment. Water transparency is monitored using a titanium–sapphire laser to illuminate a diffuser-ball light source, and measuring signals recorded by a CCD camera (see Section 8.1.2). Later in the experiment light scattering and absorption parameters are measured by a set of dye/N_2 lasers (see Section 8.2). These results can be independently checked by reconstructing tracks of through-going cosmic ray muons, which provide a line source of Cherenkov light of known characteristics.

The relative gain of individual PMTs is monitored using a scintillator ball illuminated by a Xe lamp. Relative timing is calibrated by a fast pulsed nitrogen laser light source connected to a diffuser ball. The diffuser ball is carefully designed to minimize time spread of emitted light.

In addition to elementary calibrations of PMT performance, a number of calibrations are required to fix the absolute energy scale and other parameters needed for the various physics analyses. For example, the solar neutrino data analysis requires precise knowledge of energy scale, resolution and detection efficiency for low energy (few MeV) electrons. For this purpose several independent calibration systems are used (see Section 8).

A low energy electron linear accelerator (LINAC) is used to inject a very low flux of electrons of precisely known energy into the tank at known locations. This system is summarized in Section 8.5, and has also been described in detail elsewhere [26]. As a cross-check, a deuterium–tritium neutron generator (DTG) is used to create ^{16}N, which decays producing a 4.3 MeV electron accompanied by a 6.1 MeV γ (see Section 8.6). Earlier in the experiment, a nickel–californium source was used for this purpose (see Section 8.7). Finally, stopping muons, their decay electrons, and π^0's produced by atmospheric neutrinos provide other independent modes for absolute energy calibrations (see Sections 8.8–8.10).

Online DAQ computers located in the electronics huts and nearby control room identify, build and preprocess raw event data structures. In addition, a realtime Supernova Watch computer system checks for event rate bursts which might signal a detectable supernova, warning shift duty physicists and automatically launching appropriate software. There is a "slow control" monitor that regularly check high voltage, temperatures of electronics crates and status of compensating coils. These systems are discussed in Sections 5 and 6.

From the mine, the data stream is sent over a fiber-optic network cable to an office-laboratory (*Kenkyuto* in Japanese) located in Higashi–Mozumi village, approximately 5 km from the mine tunnel entrance. The Kenkyuto houses the magnetic tape library for data archiving, a powerful cluster of computers for data reduction and analyses, and work facilities for users, including computer workstations, meeting rooms, user offices, support staff, and a library. A dormitory for users and visitors is also located in Higashi–Mozumi, which is connected by rail and highway to the city of Toyama, 30 km away.

Run control processes are used to operate the experiment from the control room in the mine. Since 2000, the experiment has also been operated remotely from the Kenkyuto. Initially, two shift physicists were on duty in the mine control room at all times during operation. By the end of Super-Kamiokande I, operation had become so smooth that this was considered unnecessary, and shift duty was reduced to one shift per day in the mine

and two shifts operated remotely from the Kenkyuto; only one duty physicist was required per shift, with backup personnel on hand nearby for safety purposes. For emergency access, a qualified mine driver (requiring special training and licensing by the Japanese mining authorities) was always on standby duty.

Run control software is used to set trigger conditions, and to break the stream of triggers into consecutively numbered runs and subruns, providing blocks of events of manageable size for bookkeeping and analysis purposes. Runs are started manually, within which subruns are automatically defined by the software. A subrun is defined as a time period of 10 min long or as 200 MB of data. As operation became more foolproof, uninterrupted runs extended in length until finally a rule was imposed that runs must be stopped after no more than 24 live-hours.

Offline processes which run continuously during data-taking are used to categorize, filter and preprocess the data stream. Events meeting appropriate cuts are routed to processing streams for the primary event categories, each with a corresponding data analysis working group: solar neutrinos, atmospheric neutrinos and nucleon decay candidates, and upward-going muons. Each of these analysis streams has its own reduction software processes. In addition, updated calibration data need to be periodically merged with existing databases. All events are saved on an automated magnetic tape library system, with the exception of downward-going muons, for which only reconstructed track parameters are saved. Offline data processing is described in detail in Section 9.

Table 2 lists for the reader's convenience a number of specialized acronyms and abbreviations which will be defined in the text.

Table 2
Acronyms used in this paper which are unique to Super-Kamiokande, or may not be universal usage in the particle physics community

Acronym	Meaning
ATM	Analog Timing Module (ID front-end electronics)
CP	Cartridge Polisher (water purification subsystem)
DTG	Deuterium–Tritium Generator (for calibration)
FSCC	Fastbus Smart Crate Controller (FASTBUS controller)
GONG	Go/NoGo Module (part of ID DAQ system)
HE	High Energy trigger (30 MeV threshold, atmospheric neutrinos)
HITSUM	analog signal proportional to number of hit PMTs, used for triggering
ID	Inner Detector
IE	Ion Exchanger (water purification subsystem)
IT	Intelligent Trigger (software trigger to filter low energy data)
LE	Low Energy trigger (6 MeV threshold)
LTC	Local Time Clock (50 Hz clock counter)
MD	Membrane Degasifier (water purification subsystem)
OD	Outer Detector
pe	Photoelectron
PMT	Photo-Multiplier Tube
QTC	Charge-to-Time converter
RO	Reverse Osmosis system (part of water purification system)
SCH	Super Control Header (part of ID DAQ system)
SDS	Sparse Data System
SLE	Super-Low Energy trigger (4.5 MeV threshold)
SMP	Super Memory Partner module (part of ID DAQ system)
TAC	Time-to-Analog Converter
TKO	TRISTAN KEK Online module
TRG	TRigger module (part of Trigger DAQ system)
Tyvek®	Reflective material used for lining OD
UF	Ultra-Filter (water purification subsystem)
VD	Vacuum Degasifier (water purification subsystem)
WS	Wavelength Shifter

3. History and construction of Super-Kamiokande

Super-Kamiokande was designed to extend and improve upon the experience gained by its scientific predecessors, the Kamiokande I–III [11] and IMB [12] experiments. Its huge scale made it the world's largest nucleon decay and solar, atmospheric and supernova neutrino detector. The detector was originally proposed by M. Koshiba and the Kamiokande Collaboration in 1984. The Super-Kamiokande Collaboration was organized as a Japan–US collaboration in 1992. The detector was built and is now operated by a collaboration of institutions from Japan and the United States. A total of about 120 physicists from 23 institutions are currently involved in the experiment.

After considering other locations within Japan, the Kamioka mine was determined to be the most suitable location for the experiment for many reasons. The Kamiokande experiment had been successfully completed and made significant physics contributions; the mine was still in operation with existing facilities (electricity, water, air ducts, drains, communications); its rock structure was well known and very stable. A suitable site was identified within the mine for the new experiment, close to the existing main tunnel; thus it would not be necessary to excavate a new tunnel, whose cost would be a substantial fraction of the total budget.

The Super-Kamiokande project was approved by the Japanese Ministry of Education, Science, Sports and Culture in 1991 for total funding of approximately \$100 M. The US portion of the proposal, which was primarily to build the OD system, was approved by the US Department of Energy in 1993 for \$3 M. In addition the US has also contributed about 2000 20 cm PMTs recycled from the IMB experiment.

Excavation of the cavity started in 1991, and detector construction was completed by December, 1995. Super-Kamiokande was successfully commissioned and began operations on April 1, 1996, as scheduled. By May 1, 1996, minor initial problems with the DAQ were cleared up and data taking began in earnest. While earlier data are valid, the large number of interrupted runs collected in April, 1996 are normally discarded for convenience in physics analyses except for analyses of upward-going muons. Fig. 3 shows the construction timeline.

A general view of the detector and other facilities is shown in Fig. 4. In the inset at the right bottom corner, a sectional view of Mt. Ikenoyama is shown, with Super-Kamiokande almost directly under the peak where the tunnels merge.

The cavity which houses the 50 kton tank is located near the mine's main horizontal truck tunnel, which is 1800 m long at approximately 350 m altitude above mean sea level, as shown in Fig. 5. The Atotsu tunnel, named after the river near its entrance, provides access to the tank top, with its electronics huts and calibration equipment, as well as the experiment control room, a separate cavity housing the water purification system, toilet facilities, and a parking area for mine vehicles. A branch tunnel winds downward around the tank and provides access to the pressure hatch at the tank bottom. Additional halls for the electron LINAC located above and behind the main tank cavity and for equipment storage are also provided.

The main tunnel also provides access to other experiments at the Kamioka Observatory such as KamLAND. As a safety backup the experimental areas can also be reached by mine train from the mine company's surface facilities in Higashi–Mozumi village.

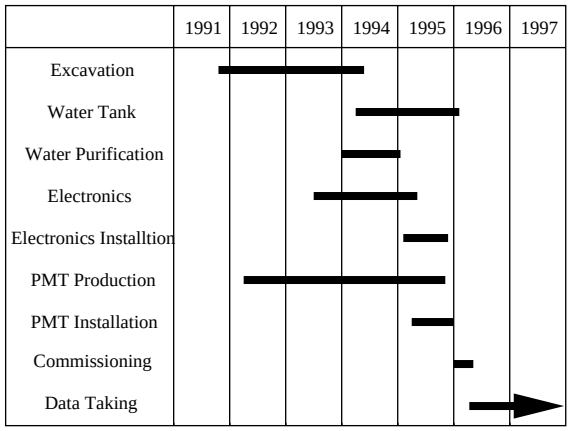

Fig. 3. Super-Kamiokande construction schedule.

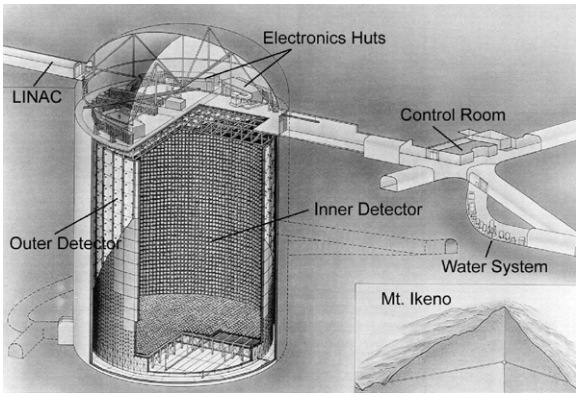

Fig. 4. A sketch of the Super-Kamiokande detector site, under Mt. Ikenoyama.

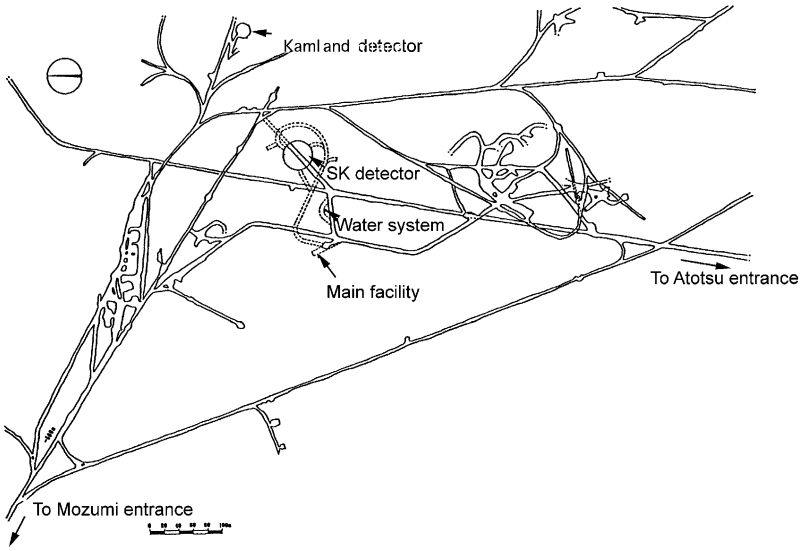

Fig. 5. Experimental environment around the detector in the mine.

4. Detector

4.1. Tank, PMTs, and associated structures

The outer shell of the detector is a cylindrical stainless-steel tank, 39 m in diameter and 42 m in height (see Fig. 6). The tank is self-supporting, with concrete backfilled against the rough-hewn stone walls to counteract water pressure when the tank is filled. The capacity of the tank exceeds 50 ktons of water.

As described previously, a cylindrical PMT support structure divides the tank into two distinct, optically isolated volumes. The structure has inner dimensions 33.8 m (diameter) by 36.2 m (height), defining the ID which contains 32 ktons of water and was viewed by 11,146 inward-facing 50 cm PMTs (Hamamatsu R3600). Approximately 2.5 m of water remain on all sides outside the support structure. This OD volume serves as an active veto counter against incoming particles as well as a passive shield for neutrons and γ rays from the surrounding rocks. It was instrumented with 1885 outward-facing 20 cm PMTs (Hamamatsu R1408), most of which were recycled from the IMB experiment. The two detector volumes are isolated from each other by two light-proof sheets on both surfaces of the PMT support structure, including top and bottom. The 55 cm thick support structure comprises a third distinct volume, a dead space from which light in principle cannot escape. The OD PMTs were mounted in water-proof housings which effectively block light from the dead space. However, because the ID PMTs were not fully covered in back, some light generated in this region was still detected by the ID PMTs.

The ID PMTs were mounted on a 70 cm grid, with 7650 on the barrel (side walls), 1748 on the top and 1748 on the bottom. Thus the effective photocathode coverage of the ID surface was 40%.

A detailed description of the 50 cm PMTs (Fig. 7) used in this experiment can be found elsewhere [13]. The bialkali (Sb-K-Cs) photocathode has peak quantum efficiency of about 21% at 360–400 nm as shown in Fig. 8. The collection efficiency for photoelectrons (pe) at the first dynode is over 70%. The 1 pe peak can be clearly seen in Fig. 9. The transit time spread for a 1 pe signal is 2.2 ns as demonstrated in Fig. 10. The average dark noise rate at the 0.25 pe threshold used in Super-Kamiokande is about 3 kHz. The ID PMTs were operated with gain of 10^7 at a supply

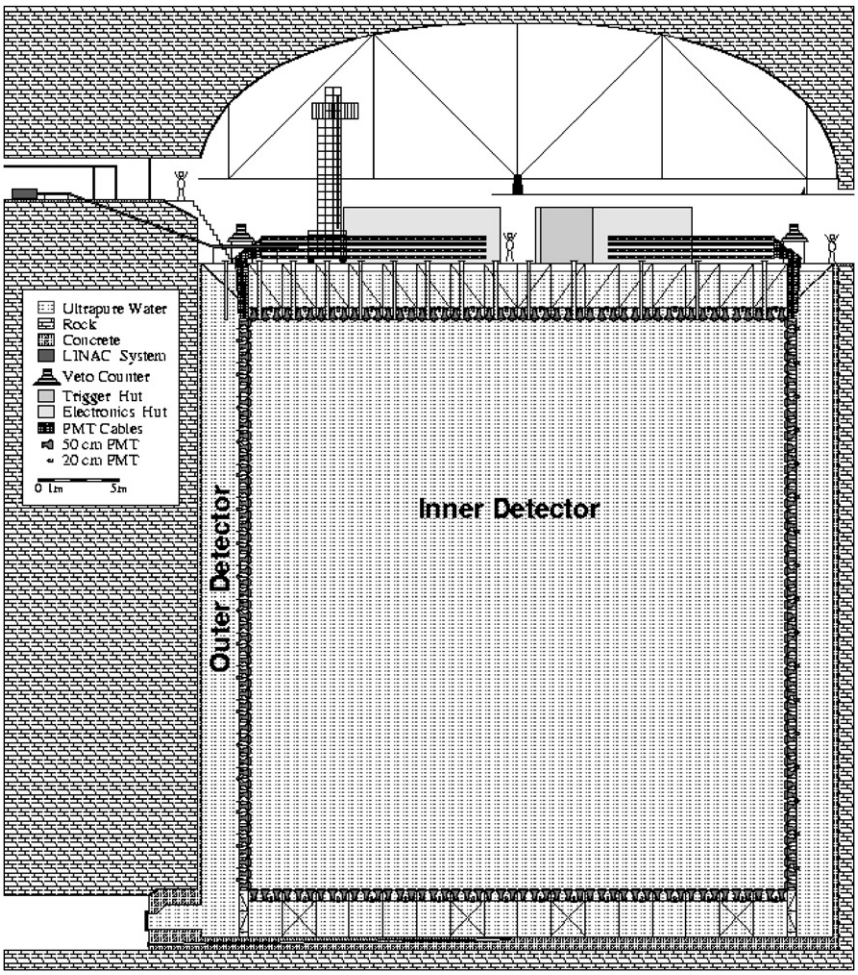

Fig. 6. A cross-section of the Super-Kamiokande detector.

high voltage ranging from 1700 to 2000 V. The neck of each PMT was coated with a silver reflector to block external light, although as noted, light can enter through the back of the hemispherical portion of the PMT.

Fig. 11 shows a detail of the support structure for the ID PMTs. All support structure components are stainless steel.

The basic unit for the ID PMTs is a "supermodule", a frame which supports a 3×4 array of PMTs. Supermodule frames are 2.1 m in height, 2.8 m in width and 0.55 m in thickness. These frames are connected to each other in both the vertical and horizontal directions. Then the whole support structure is connected to the bottom of the tank and to the top structure. In addition to serving as rigid structural elements, supermodules simplified the initial assembly of the ID. Each supermodule was assembled on the tank floor and then hoisted into its final position. Thus the ID is in effect tiled with supermodules. During installation, ID PMTs were preassembled in units of three for easy installation. Each supermodule has two OD PMTs attached on its back side. The support structure for the bottom PMTs is attached to the bottom of the stainless-steel tank by one vertical beam per supermodule frame. The support structure for the top of the tank is also used as the support structure for the top PMTs.

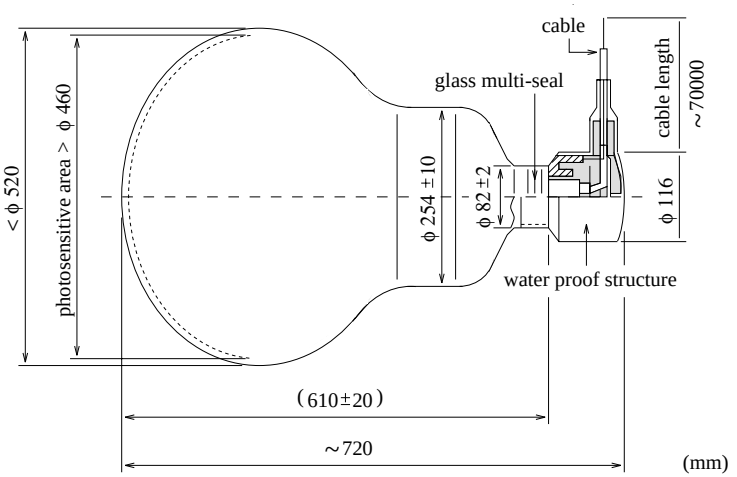

Fig. 7. Schematic view of a 50 cm PMT.

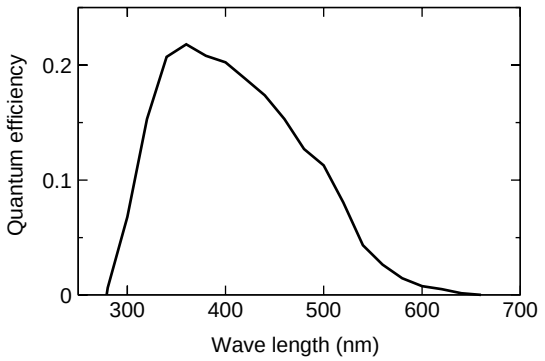

Fig. 8. Quantum efficiency of the photocathode as a function of wavelength.

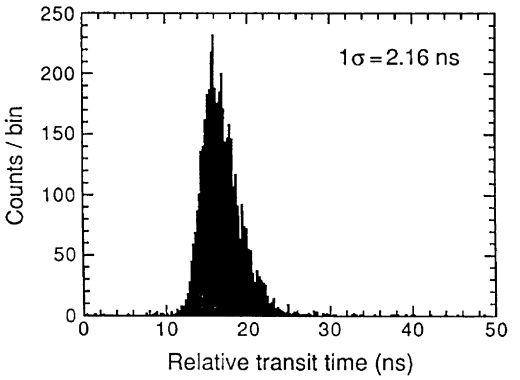

Fig. 10. Relative transit time distribution for a typical PMT tested with 410 nm wavelength light at the single photoelectron intensity level.

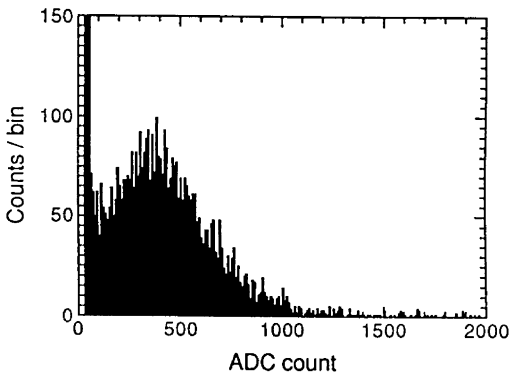

Fig. 9. Single photoelectron pulse height distribution. The peak close to zero ADC count is due to PMT dark current.

Opaque black polyethylene telephthalate sheets cover the gaps between the PMTs in the ID surface (see Fig. 11). These sheets improve the optical separation between the ID and OD and suppress unwanted low-energy events due to residual radioactivity occurring behind the PMTs. The reflectivity of the photocathode surface of PMTs and the black sheet were measured, with results shown in Fig. 12, along with the calculated values which are used in Monte Carlo simulations.

Cables from each group of 3 PMTs are bundled together. All cables run up the outer surface of the PMT support structure, i.e., on the OD PMT plane, pass through cable ports at the top of

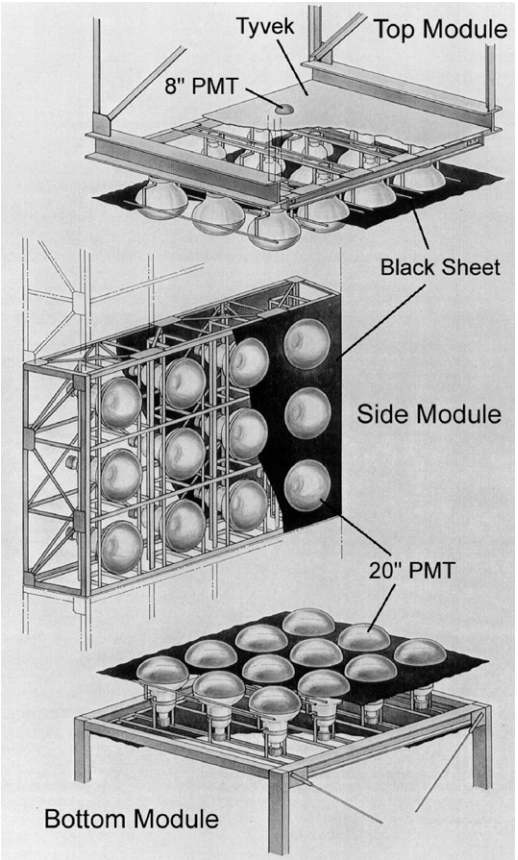

Fig. 11. Schematic view of support structures for the inner detector.

the tank, and are then routed into the electronics huts.

The thickness of the OD varies slightly, but is on average about 2.6 m on top and bottom, and 2.7 m on the barrel wall, giving the OD a total mass of 18 ktons. OD PMTs were distributed with 302 on the top layer, 308 on the bottom, and 1275 on the barrel wall.

Light collection efficiency in the OD is enhanced by WS plates attached to each OD PMT [12]. The WS plates are square acrylic panels, 60 cm on a side and 1.3 cm thick, doped with 50 mg L^{-1} of bis-MSB. The PMT is mounted into a machined hole at the center of the plate. Optical coupling is by simple physical contact between the plate and the PMT glass or partially through water. The WS plates function by absorbing UV light, and then re-radiating photons in the blue–green, better matching the spectral sensitivity of the PMT's bialkali photocathode. The light collection of the PMT plus WS unit is improved over that of the bare PMT by about a factor of 1.5.

Because the decay constant of the fluor (4 ns) is small relative to the inherent timing resolution of the OD PMTs (13 ns), the plates do not significantly degrade the timing resolution of the composite system. At single photoelectron illumination, the timing resolution is 15 ns (FWHM) with the plate, versus 13 ns without the WS [12]. This resolution is considerably poorer than the 2 ns resolution of the newer ID PMTs. However, since the design of the OD was optimized for use as a calorimeter and veto counter, rather than a particle tracker, the extra photons are of importance while the poorer timing resolution is of little consequence.

To further enhance light collection, the OD volume is lined with a reflective layer made from Type 1073B Tyvek® manufactured by DuPont. This inexpensive and very tough paper-like material has excellent reflectivity in the wavelength range in which PMTs are most sensitive, especially at short wavelengths. Measured reflectivities are on the order of 90% for wavelengths in excess of 400 nm, falling to 80% at about 340 nm [10]. The presence of this liner allows multiple reflections of Cherenkov light, which minimizes the effects of dead PMTs, given their coarse spacing in the OD. Cherenkov light is spread over many PMTs, reducing pattern resolution but increasing overall detection efficiency.

Black and white liners that define the inner surface of the OD were specially made, according to our specification, from a sandwich of Tyvek® facing the OD volume), a central layer of white Low-Density Polyethylene (LDPE) 25 μm thick, and a 25 μm layer of black LDPE. This liner material provided a reflective surface on the OD side and a black absorptive surface facing the dead space between the OD and ID PMTs. Thus these liners also serve as optical barrier for the dead space region.

The OD PMTs and WS plates were originally employed in the IMB detector [12]. The increased depth of the Super-Kamiokande detector (40 m vs

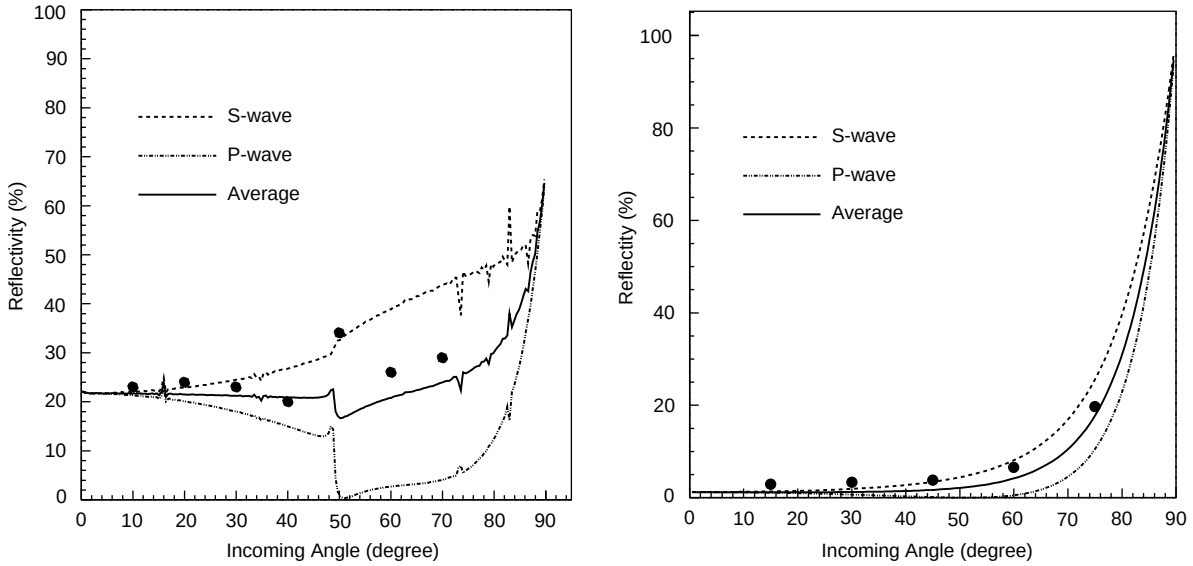

Fig. 12. Reflectivity of PMT surface (left panel) and the opaque sheets used to fill gaps between PMTs (right panel). Points show the results of measurements, and lines show calculated values: the dashed line shows the S-wave, the dotted line shows P-wave and the solid line shows the averaged value.

20 m for IMB) required a redesign of the water-tight housing which protects the PMT divider chain. A new cable feed-through system was developed and tested several times the maximum expected pressure. However, failure of feed-through system was still a major contributor to PMT losses experienced over the first 5 years of operation of the detector. After more than 5 years of operation, 261 (14%) of the OD PMTs had failed, and approximately 70% of these failures were attributed to flooding of the PMT base housing. Another 27% of the failed PMTs became "flashers", i.e., developed internal electrical discharges which emitted substantial optical radiation and electrical noise, requiring the PMT to be shut down. The remaining failed PMTs showed a variety of electrical and other problems. Just before the 2001 shutdown, OD PMTs continued to fail at a nearly constant rate of 2–3 per month. In contrast, the failure rate for ID PMTs dropped rapidly after the detector had been in operation for a few months. However, OD PMT losses were still at a level which did not significantly degrade the ODs performance.

To protect against low energy background from radon decay products in the air, the roof of the cavity and the access tunnels were sealed with a coating called Mineguard® produced by Urylon in Canada. Mineguard® is a spray-applied polyurethane membrane developed for use as a rock support system and radon gas barrier in the mining industry. Double doors in the access tunnels restrict air flow from the mine into the detector cavern. An over-pressure of "radon-free" air is piped in from the outside to further hold back contaminated mine air. The outside air contains relatively little radon since it is taken from an area away from the mine entrances. As described later, radon-reduced air is also produced in the mine and pumped into the region above the water inside the detector tank, at a slight over-pressure.

The average geomagnetic field is about 450 mG and is inclined by about 45° with respect to the horizon at the detector site. This presents a problem for the large and very sensitive PMTs which prefer a much lower ambient field. The strength and uniform direction of the geomagnetic field could systematically bias photoelectron trajectories and timing in the PMTs. To counteract this 26 sets of horizontal and vertical Helmholtz coils are arranged around the inner surfaces of the tank. With these in operation the average field in

the detector is reduced to about 50 mG. The magnetic field at various PMT locations were measured before the tank was filled with water.

To minimize anomalous response from charged particles passing close to the ID PMTs, and to further filter events due to natural radioactivity in the surrounding rock, a standard fiducial volume of approximately 22.5 ktons is defined as the region inside a surface drawn 2.00 m from the ID wall, i.e., a centered cylinder of diameter 29.8 m and height 32.2 m. Fiducial volume cuts in effect provide a further passive shield against entering events, and restrict event reconstruction to a region of minimum fitter bias.

The diagonal dimension of the ID is about 50 m, which approaches typical values of attenuation and scattering lengths for purified water. Absorption lengths in pure water are on the order of 100 m. These values are consistent with water transparency measurements in Super-Kamiokande, as described in a later section.

5. Electronics and data aquisition

5.1. ID electronics

ID PMT signals are processed by custom built TRISTAN KEK Online (TKO) [14] modules called ATMs [15]. The TKO system was originally developed and built by KEK, and is optimized for front-end electronics where a large number of channels are to be handled. The ATM has the functionality of a combined Analog-to-Digital Converter (ADC) and TDC, and records the integrated charge and arrival time of each PMT signal. Signals from 12 PMTs are fed to an ATM board. Fig. 13 shows a schematic view of the analog input block of the ATM. The PMT signal into the current splitter is divided into four signals. One of them is fed to the discriminator with the threshold level for each channel set to −1 mV, which corresponds to 1/4 pe equivalent. When the PMT signal is above the threshold level, a "hit" signal with 200 ns width and 15 mV pulse height is asserted on the ATM front panel. The HITSUM signal, which is used to generate the global trigger signal, is the analog sum of all these 15 mV/

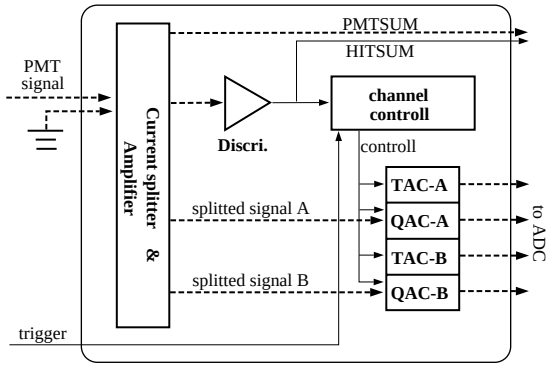

Fig. 13. A schematic view of the analog input block of the ATM. Only one channel is shown in the figure. Dashed arrows show the PMT signal, its split signals, and accumulated TAC/QAC signals. Solid arrows show the logic signals which control the processing of the analog signals.

channel pulses. At the same time, either of the split signals, A or B, is held by a Charge-to-Analog Converter (QAC) [16], and a Time-to-Analog Converter (TAC) [16] starts to integrate constant current. If a global trigger is received, the information in the TAC/QAC is digitized and stored in internal memory buffers. Since, for each channel, TAC integration is started by the PMT signal itself, the arrival time of the signal can be inferred from the value of the integrated charge. A "channel control" chip generates start/stop signals for the TAC, the gate signal for QAC, and clear signals for both. Output signals from the TAC/QAC are fed to an ADC and digitized. The ADC/TDC output data have 12 bit (4096 channel) resolution. The ATM has about 450 pC dynamic range for charge, with a resolution of 0.2 pC, and about 1300 ns dynamic range in timing, with a resolution of 0.4 ns.

There are two TACs and QACs for each channel so that events in rapid succession, such as a muon followed by its decay electron, can be processed without deadtime.

To maintain accuracy of the timing and charge information, conversion tables are used (instead of fitted linear functions) to convert ADC and TDC counts to pC and ns, respectively.

The temperature dependence of ADC and TDC pedestals (offsets) is linear and less than 3 count/°C (0.6 pC/°C) and 2 count/°C (0.8 ns/°C),

respectively, in the typical ambient temperature range. Fig. 14 shows an example of the temperature dependence of the ATMs. To correct for the temperature dependence of the ADCs and TDCs, pedestal data are taken every 30 min in Super-Kamiokande and the measured pedestal values are used to convert ADC and TDC counts within each half-hour period. Ambient temperature is kept at about $27^{\circ}C \pm 0.5^{\circ}C$ in the electronics huts. The inaccuracies introduced by temperature dependence are estimated to be less than 0.3 pC and 0.4 ns for the charge and timing information, respectively.

High voltage for each ID PMT is distributed by 48 CAEN SY527 high voltage main frames. Each SY527 main frame accommodates 10 CAEN A933 K high voltage cards which have one primary high voltage generator and 24 programmable active distributor output channels on each card. Those main frames are connected to CAENet network via 4 sets of V288 CAENet-VME interface cards to be controlled and monitored remotely by a slow control computer.

5.2. ID data acquisition

Fig. 15 shows a schematic view of the ID-DAQ system. There are a total of 946 ATM modules, located in four "quadrant huts". ATMs record

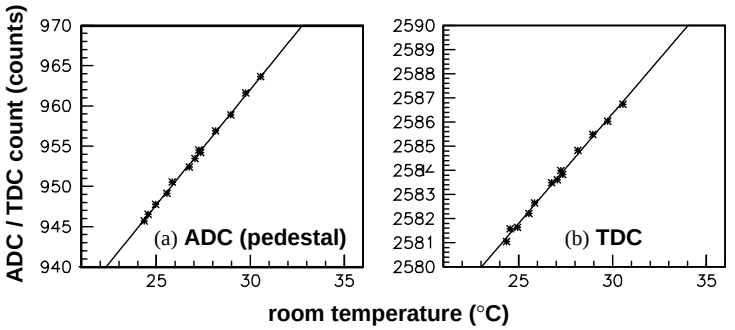

Fig. 14. The ambient temperature dependence of ADC and TDC pedestals. Both ADC and TDC show linear dependence on ambient temperature.

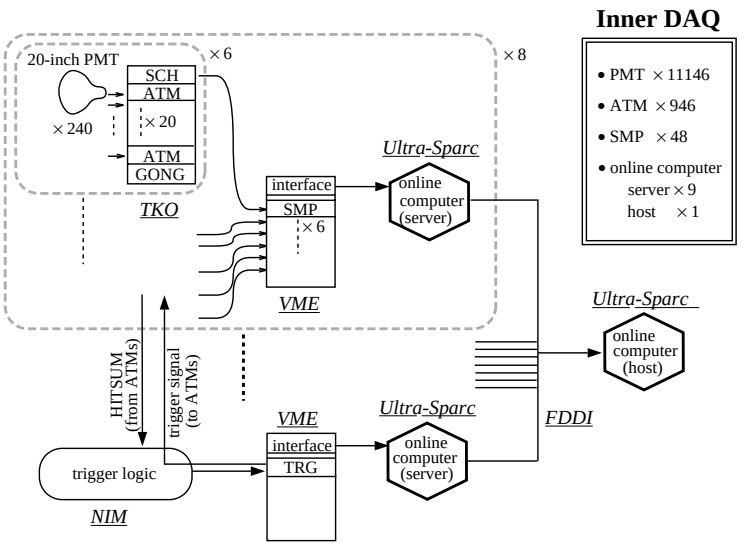

Fig. 15. The data acquisition system for the inner detector. Arrows show data flow.

ADC/TDC data of each above-threshold PMT when a global trigger signal is asserted by the VME TRG (TRiGger) module. The global trigger signal, and event number information generated in the TRG module, are distributed to all ATMs via 48 GONG (Go/NoGo) modules. ADC/TDC data stored in ATM FIFO memory are read by the Sparse Data Scan (SDS) method as described below.

SDS is a TKO-specific functionality that allows collection of all data in TKO modules without any external CPU. SDS is triggered by an external input signal on Super Memory Partner (SMP) modules every 16 events. In SDS, SMPs read all TKO data via the TKO Super Control Header (SCH) module, storing the data in one of their two switchable 1 Mbyte memories. SDS first reads a 16-bit event counter from the GONG modules, and hit PMT information (channel address, 8-bit event counter, timing data and integrated charge data) from each ATM module. Whenever 512 kB of data have been stored in one of the two memory buffers in the SMP module, or 1024 scans have been performed, the SMP module switches to the other buffer, to ensure no loss of data due to overflow.

Each on-line server (200 MHz UltraSPARC CPUs) reads event data from its share of the SMP memories via a Bit-3 Sbus-VMEbus interface using block transfer. Trigger information, i.e., the event number, the trigger time, and trigger type, are recorded in the VME TRG module, which is read by a separate server. All data collected by servers are transferred to the on-line host computer (a 300 MHz UltraSPARC CPU) via an FDDI network, and the data (including OD data) are merged by an event builder process to make a complete event record.

Data transfer speeds were studied for several specific situations. The data transfer speeds observed for (a) SMP→computer, (b) SDS and (c) TRG→computer are shown in Fig. 16.

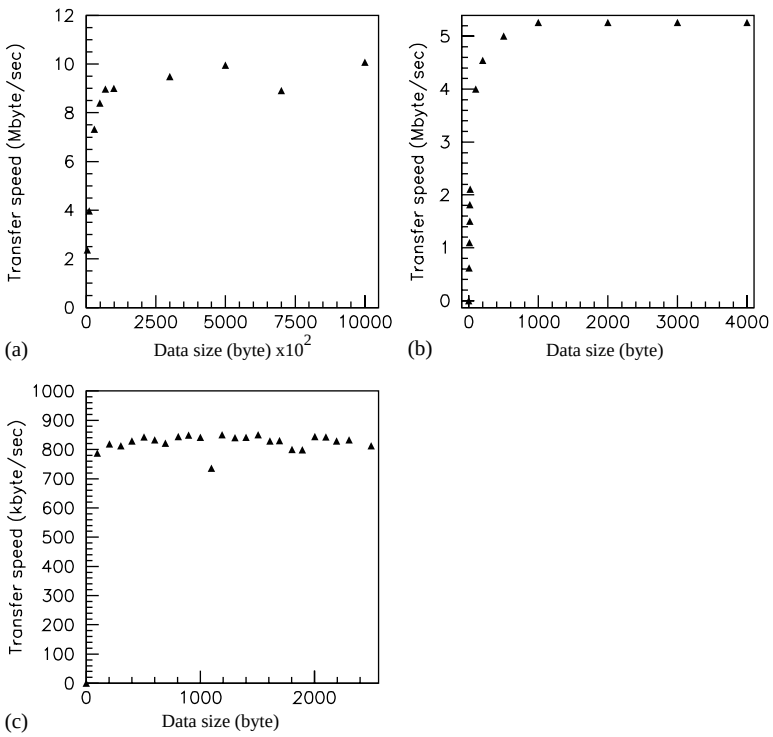

Fig. 16. Measured data transfer speed for: (a) SMP→on-line server, (b) Sparse Data Scan and (c) TRG→on-line server as a function of data size.

The actual performance of the system for supernova detection can only be estimated by the measurement of deadtime with simulated high-rate event bursts. We used the DTG calibration source described in a later section to simulate supernova neutrino bursts, since γ rays from the source have a decay time of 7 s. (A description of expected supernova neutrino burst characteristics is given in a later section on realtime supernova watch software.) Results from these deadtime measurements with several burst rates are summarized in Table 3.

All the deadtimes were measured with reference to the 1.7 kHz SLE trigger rate (see Section 5.4.2 for triggers). Here, the peak trigger rate refers to the averaged rate in the first 1 s, and the total number of events is the number of events generated within 45 s after activating the DTG. The actual number of triggered events can be obtained by multiplying the total number of events by the livetime, which equals $(1 - f_{\mathrm{dead}})$ where f_{dead} is deadtime as a fraction of the livetime. The plots on the left in Fig. 17 show the event rate variation as a function of elapsed time from the beginning of the burst. In this figure, event rates are plotted for: (a) 0.1 s binning, (b) 2 ms binning, and (c) 40 μs binning, respectively. There is no deadtime (time period without any events) in the left plot of Fig. 17(c). In fact, there were no veto signals at all in the data. The veto signal is set whenever the memory buffer of any SMP module is in danger of overflow.

Table 3
Deadtime fractions for burst trigger tests

Peak trigger rate (kHz)	Total number of events	Deadtime (%)
7.5	50,000	0
12	80,000	0
21	150,000	14
45	300,000	32
75	500,000	60

The right-hand plots in Fig. 17 show the event rate change for a 75 kHz burst. According to these plots, deadtime occurred approximately 0.1 s after the beginning of the burst. All the data for the first 0.1 s were successfully stored in the SMP module. However, if additional data fill a memory buffer

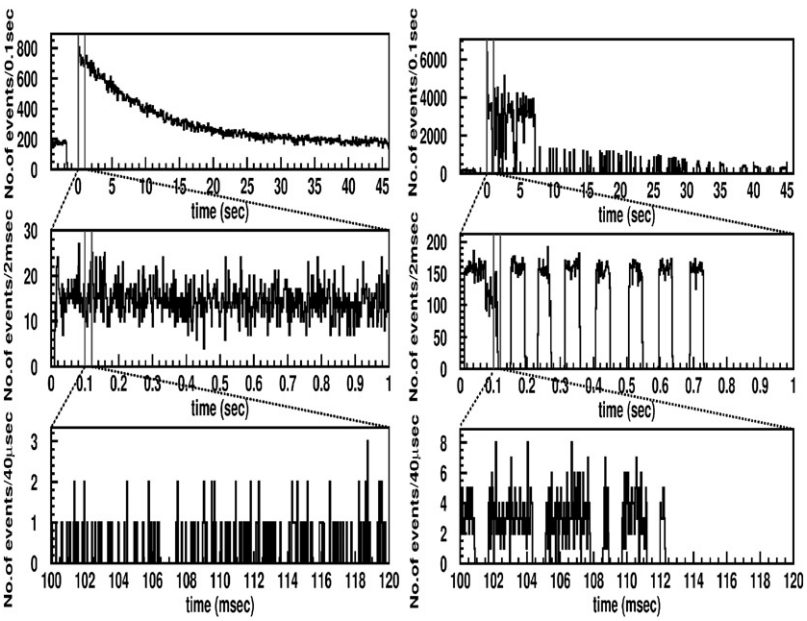

Fig. 17. Event rate variation as a function of time after beginning of a trigger burst, for 7.5 kHz burst (left), and 75 kHz burst (right). Bin sizes are (top) 0.1 s, (middle) 2 ms, and (bottom) 40 μs, respectively. No deadtime is observed for bursts up to 12 kHz. However, there are blank areas due to deadtime in the right-hand figure (middle and bottom) after 0.1 s.

while the collector process is reading data out from another memory buffer, data loss will occur, and the DAQ system may crash. To avoid this situation, the veto signal is set when 50% of the memory has been used for storing data while the collector process reads the data from another buffer. The veto signal is released after all the data have been read, and then the TRG module is re-enabled. A periodic series of deadtimes were observed in the tests, as shown in the right-hand plot of Fig. 17.

Finally, the performance of the DAQ system under a continuously high trigger rate was tested. The lowest trigger threshold in these measurements corresponded to about 3.6 MeV neutrino energy threshold, and the trigger rate was about 2.1 kHz. In these test runs, data taking continued for about 10 min without any faults. All test runs succeeded in taking data and no data pile-ups were observed in the entire on-line system. The critical point for DAQ is vertex fitting for the Intelligent Trigger (IT, described in detail in Section 5.4.2), which is limited by CPU power. However, the IT does not pose a problem for relatively brief trigger rate bursts, as expected from supernova, because the amount of data (per event and in total) to be processed is not very large.

The ID-DAQ system thus performs well not only for high rate bursts but also in a continuous high trigger-rate environment. The tests confirmed that Super-Kamiokande can take data without loss (i.e., with negligible deadtime) during the type of neutrino event bursts expected from a galactic supernova located as close as 2–3 kpc from the Earth. Super-Kamiokande can also take data continuously at a 2.1 kHz trigger rate, which corresponds to a 3.6 MeV total energy threshold with 50% efficiency.

5.3. OD electronics and DAQ

A block diagram of the OD-DAQ system is shown in Fig. 18. As with the ID, signals from the PMTs are processed and digitized in each of 4 quadrant electronics huts. From there, the signals are picked off, digitized and stored. As in the ID, local HITSUM pulses are formed in each quadrant hut and sent to the central hut, where their analog sum creates an OD trigger signal when the OD HITSUM threshold is exceeded. Fig. 18

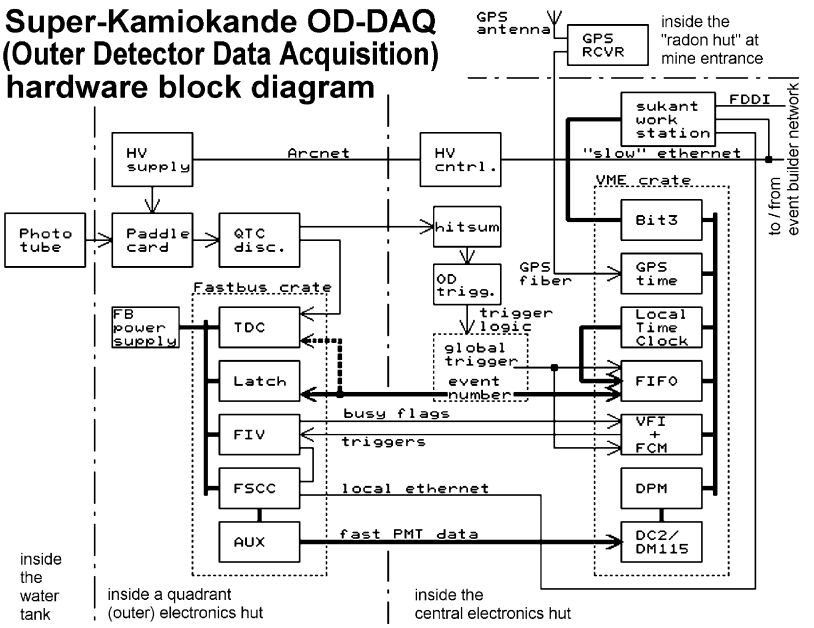

Fig. 18. OD DAQ block diagram and data flow.

illustrates the data flow in a quadrant hut as well as the overall data flow. When a trigger from any source occurs, the data are passed out of the quadrant huts to the central hut for further processing.

The OD PMT cables are fed into the quadrant huts. A single coaxial cable feeds high voltage to each PMT and carries back its analog signals. The OD PMTs are operated at approximately 1800 V. High voltage is distributed by a set of 4 LeCroy 1454 High Voltage Mainframes, one in each of the 4 quadrant huts. Each HV mainframe controls 48 channels of high voltage, although only 40 channels are actually used. Each channel is connected to a custom "paddle card" which fans out the voltage to 12 PMTs. The mainframes are connected to an ARCNET network, with a node in a VME crate in the central hut. This allows the high voltage to be set and monitored via a computer (the "slow-control" computer, which also operates other housekeeping functions) in the control room.

The paddle cards distribute high voltage from each of the HV mainframe channels to 12 PMTs. These cards also pick off the analog PMT signals through a high voltage capacitor and resistor network, allowing a single cable to be used for both HV and signal. In early 2001, the original paddle cards were replaced with upgraded models, which include HV relays to simplify disabling dead or noisy channels, zener diode jumpers to fine-tune HV levels for individual PMTs, and front-panel signal test points.

Once the PMT signals have been picked off from the paddle cards, coaxial ribbon cables feed them to custom charge-to-time conversion modules (QTC, see Fig. 19). The purpose of these modules is to measure the hit time and charge of the PMT pulse and convert it to a form which can be easily read and stored by the TDCs. The output of the QTC modules is a logic pulse (ECL level) whose leading edge marks the hit arrival time and whose width represents the integrated charge Q of the PMT pulse.

The block diagram of a QTC module is shown in Fig. 19. The PMT pulse is fed to a LeCroy MQT200 charge-to-time converter. This chip integrates the PMT pulse and outputs a pulse with a length proportional to the PMT charge. The MQT200 is provided with an integration gate which is generated by a one-shot fired when the PMT pulse exceeds the threshold. Thus the QTCs are self-triggering. The gate is 200 ns wide and the PMT pulse is delayed 50 ns to fall inside the

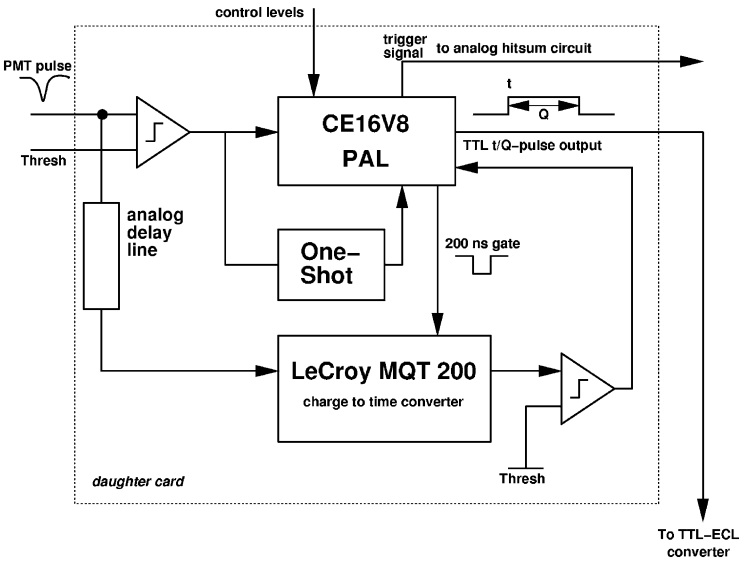

Fig. 19. Block diagram for a single QTC module.

integration gate. The output pulse of the MQT200 is discriminated and converted to a TTL pulse using a Programmable Array Logic (PAL). Then the TTL pulse is finally converted to ECL for output. Each QTC channel was tested against a standard ADC using test pulses that simulate PMT signals over a range from 0 to 200 pe.

The ECL pulses from the QTCs are fed to LeCroy 1877 Pipeline TDCs, where times for all leading and trailing edges are recorded. Each TDC module has 96 input channels (1 per PMT), with 5 TDC modules per Fastbus crate and 1 Fastbus crate in each electronics hut, providing a total capability for 1920 TDC channels.

Each TDC channel works as a circular buffer that can store up to 8 QTC pulses with a resolution of 0.5 ns over a window of up to 32 μs width. If more than 8 PMT pulses occur during a TDC window, then only the last 8 pulses are recorded and any earlier ones are lost. The window of OD data taking originally was 32 μs wide and centered about the global detector trigger time (16 μs before and 16 μs after the global trigger). In September, 1996, the window was shortened to 16 μs, with 10 μs before and 6 μs after the global detector trigger time. This shift reduced the average size of event blocks, which were padded with irrelevant out-of-time noise edges, but also reduced the probability of an overflow of the circular TDC buffers to negligible levels.

All TDC channels are digitized and read out simultaneously following a fixed delay (6 μs) after a global detector trigger. During digitization, which can take 2–15 μs depending on the number of edges in the event, the OD electronics cannot record new data (busy/in-progress deadtime), but after read-out the channels are free to take new data. If a global trigger signal is received during OD deadtime, a flag bit is introduced into the data stream to record this condition.

The TDC signals are read by a Fastbus Smart Crate Controller (FSCC) which sends the data to the central hut via a 32-bit RS485 data cable. In the central hut, the data pass through a Motorola DC2/DM115 slave CPU in the OD-DAQ VME crate and are stored in a large VME dual-port memory buffer (DPM). The two ports of the DPM eliminate data loss due to pileup when events follow one another in rapid succession. One DC2/DM115 module and 2 DPM modules are used for each quadrant's TDC data. The OD-DAQ VME crate is controlled by an online computer, a Sparc20 workstation, via a Bit3 VME-SBus interface.

The OD-DAQ software runs on the online computer. First, a "collector" process reads out the PMT data from the DPM modules, along with local time stamps from a 50 MHz Local Time Clock (LTC) counter as well as accurate UTC time from a GPS receiver set. The detector event number and other status bits are also folded in. Then, a "sorter" process merges the quadrant data event-by-event, adds the time stamps and other event information and formats the data into standard data banks. Finally, the completed OD event data are transmitted by a "sender" process, via FDDI network, to the event builder process, which runs on an online host CPU in the control room. There, the OD data are merged with ID event data to form a completed full detector event, which is transmitted to the offline processes in the Kenkyuto.

5.4. Triggers

5.4.1. Hardware trigger

Each ATM module generates a HITSUM signal of height proportional to the number of active channels. These signals are analog-summed, first by quadrant and then overall, to generate the ID HITSUM signal. Initially, there were two types of trigger signal derived from the ID HITSUM. The low energy (LE) trigger is generated when HITSUM crosses a threshold of −320 mV, and the high energy (HE) trigger has a threshold level of −340 mV. The LE trigger corresponds to 29 hit ID PMTs within a 200 ns time window, after subtracting the average dark background rate. This is equivalent to the signal expected when 50% of the Cherenkov photons generated by 5.7 MeV electron are detected. Unless otherwise stated, the term trigger threshold will be used here to mean the threshold at which the trigger efficiency is 50%. In May, 1997, the Super-Low Energy (SLE) trigger, whose threshold corresponds to 4.6 MeV, was implemented. A detailed description of the SLE trigger is given in the next section.

A similar procedure is used to generate an OD trigger, which is the only trigger that includes OD information. The QTCs generate a 20 mV by 200 ns square pulse each time a PMT pulse exceeds the threshold, which is set to −25 mV, corresponding to 0.25 pe. The threshold for the OD trigger corresponds to 19 hit OD PMTs in a 200 ns coincidence window. When an OD trigger is detected, it is held for 100 ns to see if a coincident ID trigger occurs. If an independent ID trigger does not occur within this interval, the OD alone will trigger readout of the full detector.

These four types of trigger signals (SLE, LE, HE, and OD) are fed into the hardware trigger module (TRG). In addition there are inputs for externally imposed trigger types, such as calibration (CAL), Veto Start, Stop, etc. If any one of the trigger signals is asserted, the TRG module generates a global trigger signal and a 16-bit event number, which are distributed to all quadrant huts to initiate DAQ for the current event. The TRG module also records the trigger types asserted (multiple coincident types are allowed), trigger time with 20 ns accuracy, and event number. The trigger data stored in the TRG module are read by a separate online computer and sent to the online host computer, to be merged with the PMT data. The event number is used for identification, and allows the event builder process running on the online host to assemble pieces of the event data sent by various servers.

5.4.2. Intelligent trigger

One of the original design goals of Super-Kamiokande called for a 5.0 MeV solar neutrino analysis threshold. When Super-Kamiokande began data taking in 1996, the LE trigger threshold was 5.7 MeV, while the threshold down to which the resulting data could be reliably analyzed was 6.5 MeV. Since the ^{8}B solar neutrino flux remains near its peak value below 5.5 MeV, there was a clear need to further lower the threshold.

The rate of background events rises sharply as the threshold is dropped. This is the result of a number of factors, including γs from the rock surrounding the detector, radioactive decay in the PMT glass itself, and radon contamination in the water. All rates increase as the trigger threshold is lowered, and in fact the hardware trigger rate of Super-Kamiokande increases by approximately an order of magnitude for each MeV by which this threshold is reduced. The analysis threshold was initially set at 6.5 MeV because the original offline DAQ system could only handle a maximum steady-state trigger rate of about 30 Hz.

In special data sets taken with the SLE threshold, events had their vertices concentrated at the perimeter of the ID, outside the nominal 22.5 kton fiducial volume. Therefore, it was clear that if it were possible to reliably reconstruct SLE events online and reject those with vertices outside the fiducial volume, it should be possible to drastically reduce the proportion of background events which clutter the data stream.

In late 1996, realtime software was developed to perform a double vertex fit using two different fitter algorithms, known to have different systematics, so that only those SLE events which fall within the 22.5 kton fiducial volume according to both fitting routines are kept. The fitting software runs on a dedicated dual–CPU 200 MHz Sun UltraSPARC 2200 computer. Event-by-event fit information is sent to the reformatter machine(s) (see Section 9). The reformatter machine (which converts the raw data provided by the event builder to ZEBRA format before sending it to the offline system) matches the fit information to the raw events and discards SLE triggers with fits outside the fiducial volume (except for a small prescaled sample). This software filtering procedure is called the IT.

The IT system was implemented in May, 1997. At that time the Super-Kamiokande hardware trigger threshold was lowered from 5.7 to 4.6 MeV, with a corresponding increase in raw trigger rate from 10 Hz (of LE, HE, and OD triggers) to 120 Hz.

The 110 Hz of SLE triggers were filtered by the fast IT computer, while the 10 Hz of conventional triggers were passed out of the mine unaltered. The SLE triggers were reduced by a factor of 24 (i.e., 4.6 Hz of SLE events survived). Thus a total event rate of 14.6 Hz was transmitted for offline reduction and analysis. Since the SLE events contain comparatively few active PMTs (about 70 vs about 7000 for a typical muon event), the total volume of

Super-Kamiokande data flow with filtered SLE data was only increased by 10%, even though the detector trigger rate had been increased by 1100%.

The efficiency and reliability of the IT system was checked with both calibration sources and Monte Carlo data, and is continuously monitored using prescaled samples of real, unfiltered SLE triggers. The rate of rejection for valid events over 4.5 MeV is small, $\sim 1\%$.

In 1999, and again in 2000, the IT system was upgraded with additional CPUs. By the end of Super-Kamiokande I, a total of 12 dedicated CPUs (six dual-CPU 200 MHz Sun UltraSPARC 2200s, and six custom-built dual-CPU 600 MHz Pentium III PCs running LINUX) provided 100% triggering efficiency at 4.5 MeV, and 97% efficiency at 4.0 MeV. New error–correction codes raised SLE livetime to 99.99%.

Fig. 20 dramatically demonstrates the effect of the IT system on the data collection rate. Changes in slope correspond to the sequential IT upgrades described. Super-Kamiokande's raw trigger rate has been raised over 15,000% since data taking began in 1996, but due to the IT, the rate of writing data to tape increased by less than a factor of two.

Table 4 shows the history of the IT as a function of time.

5.5. Global positioning system

Synchronization of absolute times of events with other sites is critical for the K2K (KEK to Kamioka) long-baseline neutrino beam experiment which uses the Super-Kamiokande detector, and for supernova candidates to coordinate a global "Supernova watch" program. For these purposes, accuracy of 100 ns or better is sufficient. Such accuracy is readily achieved at relatively low cost by the time synchronization system used in Super-Kamiokande. In addition to geographic coordinates, the GPS operated by the US government allows general users to obtain highly accurate absolute times, directly referable to Universal Time (UTC) as provided by the US Naval Observatory Master Clock. A low-cost commercial GPS receiver can thus fix its internal clock's UTC time offset with higher accuracy than required by Super-Kamiokande.

Two independent GPS receivers are mounted inside the radon hut (see Section 7.2) located near the entrance to the Atotsu tunnel to the Super-Kamiokande tank. These receivers are from different manufacturers (a Truetime model XL receiver, and a Motorola Model UT-Plus Oncore receiver module mounted on a custom made support board), with independent internal data

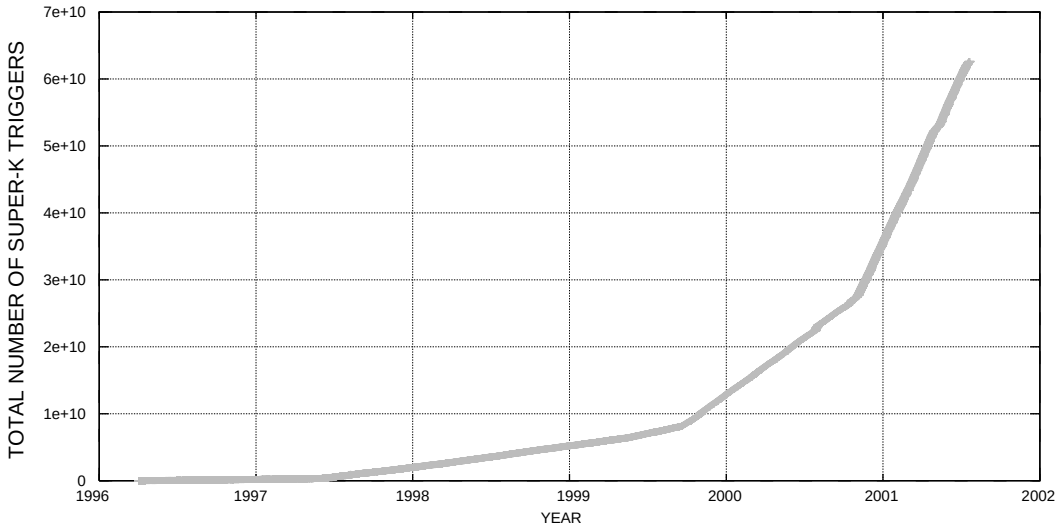

Fig. 20. The total number of triggers in Super-Kamiokande since the beginning of the experiment. The points at which the trigger rate increased due to installation of additional IT CPUs in 1997, 1999 and 2000 are quite evident.

Table 4
History of the intelligent trigger

Start date	Number of IT machines	Online trigger rate (Hz)	Filtered trigger rate (Hz)	Hardware threshold (MeV)	Analysis threshold (MeV)	SLE livetime (%)
4/96	0	10	10	5.7	6.5	0
5/97	1	120	15	4.6	5.5	96.5
2/99	2	120	15	4.6	5.5	99.3
9/99	6	580	43	4.0	5.0	99.95
9/00	12	1700	140	3.5	4.5	99.99

processing systems and software. Their antennae are mounted on top of the radon hut roof. Although the radon hut is located in a mountain valley, the portion of the sky in view is sufficient to ensure an adequate supply of satellite fixes at all times. After the receivers have operated for about 24 h, fixing their geographic location to high accuracy, only one satellite needs to be in view to maintain high accuracy timing. Each receiver produces two outputs of interest: an ASCII data stream containing time of year (DDD:HH:MM:SS) and housekeeping data, and a 1 pulse-per-s (1PPS) analog square pulse signal whose leading edge is aligned with the GPS seconds roll-over.

Both receivers transfer time information to the central hut in the mine via a dual 2 km optical fiber cable through the Atotsu tunnel. There, the signals are picked up by an interface board in the OD-DAQ VME crate in the central hut on top of the Super-Kamiokande tank. The primary TrueTime receiver uses standard IRIG-B pulse code for the optical fiber data transfer, which contains time along with status information. For the secondary Motorola receiver, a custom-made optical fiber interface module multiplexes the serial time/position/status data with the GPS 1PPS synchronization pulse before it is converted to optical pulse code.

At the OD VME crate in the central hut, the optical pulses are converted back to digital electrical signals and decoded. The TrueTime IRIG-B code is used for synchronizing and conditioning an internal clock in the TrueTime VME-SG (fiber interface) module with the GPS time to achieve 100 ns accuracy. The Motorola serial data are buffered for direct access via VMEbus by the OD-DAQ online computer. The 1PPS pulses of the two optical signals are decoded and then used as calibration triggers for a LTC module, which is basically a free-running 50 MHz clock. High-resolution time information then can be acquired via the VMEbus by the OD-DAQ online software.

Time-stamps for each OD trigger are obtained by logging the LTC count whenever a trigger occurs. The LTC is also latched whenever a 1PPS leading edge is detected so that LTC counts at GPS seconds roll-overs are also logged. A running average of the LTC oscillator count rate over 300 s is maintained to obtain a current corrected mean LTC rate. The number of LTC counts since the last seconds roll-over is multiplied by the current running average LTC rate to obtain the fraction of a second associated with each event's time-stamp, modulo the latest DDD:HH:MM:SS from the ASCII data stream, with 20 ns precision. Overall accuracy, obtained by comparing performance of the two clocks, is about 60 ns. As SLE trigger events produced by the IT system do not generate an OD trigger, their times are derived by interpolation using CPU clock data.

An essentially identical GPS system (except for the optical fiber link) was set up at KEK for the K2K long baseline neutrino oscillation experiment. Further details about the Super-Kamiokande and K2K GPS time synchronization systems can be found elsewhere [19].

6. Monitoring systems

6.1. Online monitor system

An online monitor computer located in the control room reads data from the DAQ host

computer via an FDDI link. It provides shift operators with a flexible tool for selecting event display features, makes online and recent-history histograms to monitor detector performance, and performs a variety of additional tasks needed to efficiently monitor status and diagnose detector and DAQ problems. Events in the data stream can be skimmed off and elementary analysis tools can be applied to check data quality during calibrations or after changes in hardware or online software.

6.2. Realtime supernova monitor

As demonstrated by the observation of a neutrino burst from SN1987A by Kamiokande [17] and IMB [18], a large water Cherenkov detector is a powerful tool to study the mechanism of supernova explosions in detail. To detect and identify such bursts as efficiently and promptly as possible Super-Kamiokande is equipped with an online supernova monitor system.

About 10,000 total events are expected in Super-Kamiokande for a supernova explosion at the center of our Galaxy. Super-Kamiokande can measure a burst with no dead-time, up to 30,000 events within the first second of a burst, as described in Section 5.2. A large sample of events is important for finding the direction to the supernova as described later, investigating neutrino oscillations [20], the stellar core collapse mechanism, and in particular obtaining evidence of black hole formation [21]. Super-Kamiokande with its realtime supernova search system is connected via an international supernova-watch network to other neutrino experiments.

Theoretical calculations of supernova explosions [22] suggest that neutrinos are emitted over a total time-scale of tens of seconds with about a half of them emitted during the first one or two seconds. The neutrino energy spectrum is eventually softened as the proto-neutron star cools. Exploiting these features, we search for event clusters in specified time windows of 0.5, 2 and 10 s. LE triggered data are independently passed to a realtime SN-watch analysis process every 2 min, and the process completes the analysis typically in 1 min. To save computing time, noise reduction filters similar to those used for solar neutrino analyses are applied after the timing cluster search. The thresholds for this cluster search are set to 15, 32, and 103 events per cluster, respectively, in the three time windows. Once a candidate cluster is found, the noise reduction filters are applied to the candidates and a final timing cluster search is performed. The thresholds of the final search are set to 7, 8 and 13 events, respectively, with an energy threshold of about 6.5 MeV. If the number of events in any time window exceeds the threshold, all events within 20 s are tagged as members of a burst candidate, and a "silent" flag is set so that the burst candidate can undergo subsequent offline analysis by experts.

When supernova (SN) event candidates are found, R_{mean} is calculated if the event multiplicity is larger than 16, where R_{mean} is defined as the average spatial distance between events, i.e.

$$R_{\mathrm{mean}} = \frac{\sum_{i=1}^{N_{\mathrm{multi}}-1} \sum_{j=i+1}^{N_{\mathrm{multi}}} |r_i - \mathbf{r}_j|}{N_{\mathrm{multi}} C_2}. \quad (1)$$

Neutrinos from supernovae interact with free protons, producing positrons which are distributed so uniformly in the detector that R_{mean} for SN events should be significantly larger than for ordinary spatial clusters of events, such as would be produced by spallation products. In the Super-Kamiokande detector, R_{mean} for uniformly distributed Monte Carlo events shows that no tail exists below $R_{\mathrm{mean}} \leqslant 1000$ cm. For the "alarm" class of burst, the events are required to have $R_{\mathrm{mean}} \geqslant 900$ cm for $25 \leqslant N_{\mathrm{multi}} \leqslant 40$ or $R_{\mathrm{mean}} \geqslant 750$ cm for $N_{\mathrm{multi}} > 40$. These thresholds were determined by extrapolation from SN1987A data.

Burst candidates meeting "alarm" criteria generate a signal to a realtime alert process, which prompts investigation by the shift operator, and alerts the supernova network server. The shift physicist runs special processes to check for spallation muons, the reconstructed vertex and its goodness of fit, as well as the PMT hit pattern, and makes a preliminary decision within 10 min to proceed further. If the burst candidate passes these checks, the data will be reanalyzed using an offline process and a final decision will be made within a few hours. During the Super-Kamiokande I running, this never occurred.

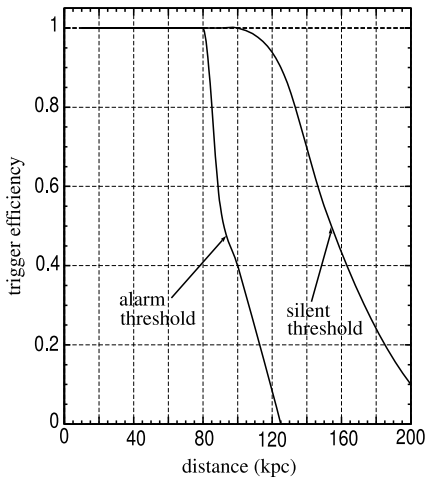

Fig. 21. Detection efficiency as a function of the distance.

Fig. 21 shows the detection efficiency as a function of the distance to the supernova for two kinds of event classes. 100% efficiency can be maintained for neutrino bursts from a supernova at a distance of up to $\sim$100 kpc if we assume the supernova has 15 times the solar mass.

One of the important capabilities of the Super-Kamiokande detector is to reconstruct the direction to supernova. By neutrino–electron scattering, $\nu_x+e^- \rightarrow \nu_x+e^-$, a total of 100–150 events are expected in case of a supernova at the center of our Galaxy. As the recoil electron via this reaction tends to be scattered in the direction of the incident neutrino, the direction to the supernova can be measured with an angular resolution

$$\delta\theta \sim \frac{30^\circ}{\sqrt{N}} \quad (2)$$

where N is the number of events produced by the $\nu-e$ scattering. The angular resolution, therefore, can be as good as $\delta\theta \sim 3^\circ$ for a supernova at the center of our Galaxy.

The Super-Kamiokande detector is thus able to provide not only the time profile and the energy spectrum of a neutrino burst, but also information on the direction to the supernova. When appropriate, the information may be forwarded to other operating neutrino experiments and astronomical observatory networks.

6.3. Slow control monitor

As part of the online monitor system, a process called the "slow control" monitor watches the status of the HV systems, the temperatures of electronics crates and the status of the compensating coils used to cancel the geomagnetic field. When any deviation from norms is detected, the physicists on shift duty are alerted, and prompted to investigate, take appropriate action, or notify experts.

6.4. Offline process monitor

A sophisticated set of software was developed to monitor and control the offline processes that analyze and transfer data. This monitor makes the complicated semi-realtime operation of the data transfer and offline data analysis processes easier to monitor and control, allowing non-expert shift physicists to identify and repair common problems to minimize down time. This software package was a significant contribution to the smooth operation of the experiment and its overall high livetime efficiency for data taking.

7. Water and air purification systems

7.1. Water purification system

The water purification system was modified and improved over the course of Super-Kamiokande I. A schematic view of the water purification system as of early 2002 at Super-Kamiokande is shown in Fig. 22.

The 50 ktons of purified water in the Super-Kamiokande tank is continuously reprocessed at the rate of about 30 tons h^{-1} in this closed cycle system. The same purification procedure is used when refilling the tank, but raw mine water is recycled through the first step (particle filters and RO) for some time before other processes, which involve expensive expendables, are imposed.

Initially, water from the Super-Kamiokande tank is passed through nominal 1 μm mesh filters to remove dust and particles, which reduce the transparency of the water for Cherenkov photons,

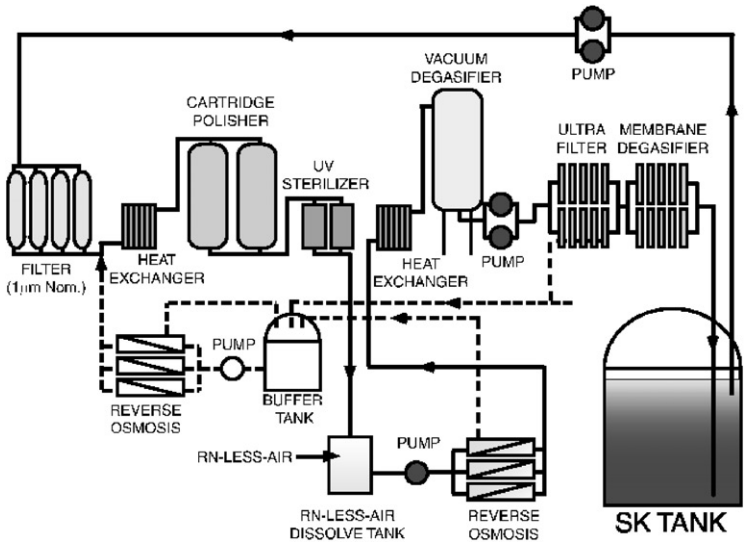

Fig. 22. A schematic view of the water purification system.

and provide a possible radon source inside the Super-Kamiokande detector.

The heat exchanger is used to cool the water to reduce PMT dark noise levels, and suppress growth of bacteria, which also reduce water transparency. Surviving bacteria are killed by the UV sterilizer stage. Typical water temperatures before the first heat exchanger and after the second heat exchanger are 14.2°C and 12.9°C, respectively.

A cartridge polisher (CP) eliminates heavy ions which also reduce water transparency and include radioactive species. The amount of CP resin used is 1500 L. Originally, an ion-exchanger (IE) column was included in the water purification system. However it was found that the IE resin was a significant radon source and it was removed.

The typical resistivity of the recirculating input water (i.e., water flowing from the Super-Kamiokande tank to the water purification system) is 11 MΩ cm. After the CP module the resistivity of the water is 18.24 MΩ cm, approaching the chemical limit.

A RO system, and a tank to dissolve Rn-reduced air (see following Section) into the water, were installed in March 1999. The RO step removes additional particulates. The introduction of Rn-reduced air into the water increases radon removal efficiency in the vacuum degasifier (VD) stage which follows.

A VD removes dissolved gases in the water. It consists of a cylindrical stainless steel vessel and a vacuum pump (16 Torr, 410 $m^3 h^{-1}$, 11 kW). The vessel is 1.4 m in diameter and 4.5 m in height. Radon gas dissolved in water is a serious background event source for solar neutrinos in the MeV energy range, while dissolved oxygen encourages growth of bacteria in the water. The typical concentration of the dissolved oxygen after the VD is 0.06 mg L^{-1}. The removal efficiency for radon gas is estimated to be about 96%.

The ultra filter (UF) consists of hollow fiber membrane filters. The minimum particle size which the UF can remove corresponds to molecular weight approximately 10,000 (or about 10 nm diameter). The typical number of particles of size greater than 0.2 μm in the water before the purification system is 1000 particles/cc; this is reduced to 6 particles/cc after purification.

A membrane degasifier (MD) also removes radon dissolved in water. It is made of 30 hollow fiber membrane modules and a vacuum pump. A flow rate of 30 L min^{-1} of Rn-reduced air from the air purification system is supplied to the MD system as purge gas. The typical pressure in the MD system is 2.6 kPa. The typical concentration

of dissolved oxygen after the MD is $0.3\,\mathrm{mg\,L^{-1}}$. The measured removal efficiency for radon is about 83%.

Radon concentrations are monitored by several realtime radon detectors. Details of the radon detector and radon measurement were previously reported [23–25]. In June, 2001 typical radon concentrations in water coming into the purification system from the Super-Kamiokande tank were $<2\,\mathrm{mBq\,m^{-3}}$, and in water output by the system, $0.4\pm0.2\,\mathrm{mBq\,m^{-3}}$.

7.2. Air purification system

Purified (Rn-reduced) air, is supplied to the gap between the water surface and the top of the Super-Kamiokande tank. The Rn-reduced air is kept at a slight overpressure to help prevent ambient radon–laden air from entering the detector. A schematic view of the air purification system is shown in Fig. 23. It consists of three compressors, a buffer tank, dryers, filters, and activated charcoal filters. A total of $8\,\mathrm{m^3}$ of activated charcoal is used. The last 50 L of charcoal is cooled to -40°C to increase removal efficiency for radon. Typical flow rates, dew point, and residual radon concentration are $18\,\mathrm{m^3\,h^{-1}}$, -65°C ($@+1\,\mathrm{kg\,cm^{-2}}$), and a few $\mathrm{mBq\,m^{-3}}$, respectively.

As noted previously, the surface of the Super-Kamiokande dome cavity above the tank is coated with radon-tight plastic material manufactured by Mineguard®. Air collected from outside the mine, with intake far from the mine entrance, is pumped into the cavity dome, as described below. Typical radon concentration in the dome air is measured to be $40\,\mathrm{Bq\,m^{-3}}$.

Radon levels in the mine tunnel air, near the tank cavity dome, typically reach 2000–$3000\,\mathrm{Bq\,m^{-3}}$ during the warm season, from May until October, while from November to April the radon level is approximately 100–$300\,\mathrm{Bq\,m^{-3}}$. This annual variation is apparently due to a chimney effect in the ventilation pattern of the mine tunnel system; during the cool season, fresh air flows into the Atotsu tunnel entrance and has a relatively short path through exposed rock before reaching the experimental area, while during the summer, air flows out the tunnel, drawing radon-rich air from deep within the mine past the experimental area. Fig. 24 shows a typical radon monitor plot recorded over one year in 2000.

The upper plot (solid line) in Fig. 24 shows levels in the tunnel outside the Super-Kamiokande cavity. The lower curve (dashed) shows levels inside the cavity, in the control room.

To keep radon levels in the dome area and water purification system below $100\,\mathrm{Bq\,m^{-3}}$, fresh air is continuously pumped at approximately $10\,\mathrm{m^3\,min^{-1}}$ from outside the mine through an air duct along the 1.8 km Atotsu tunnel to the experimental area. This flow rate generates a slight over-pressure in the Super-Kamiokande experimental area, minimizing the entry of ambient mine air. A "Radon Hut" (Rn Hut) was constructed near the Atotsu tunnel entrance to house equipment for the dome air system: a 40 hp air pump with $10\,\mathrm{m^3\,min^{-1}}$/15 PSI pump capacity, air dehumidifier, carbon filter tanks, and control electronics. Fresh air from an intake (initially located at the Rn Hut) is fed into the air pump, and is then pumped through a dehumidifier, a carbon filter tank, and finally through a 1.8 km air

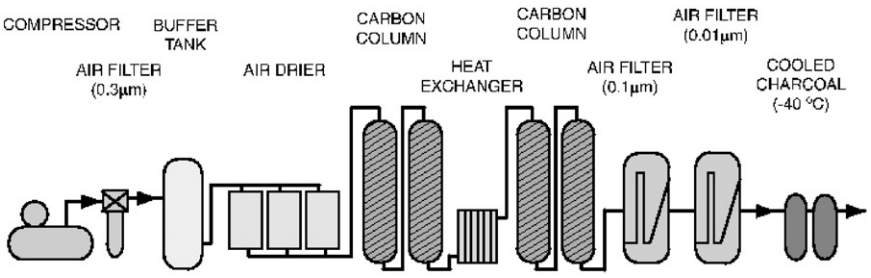

Fig. 23. A schematic view of the air purification system.

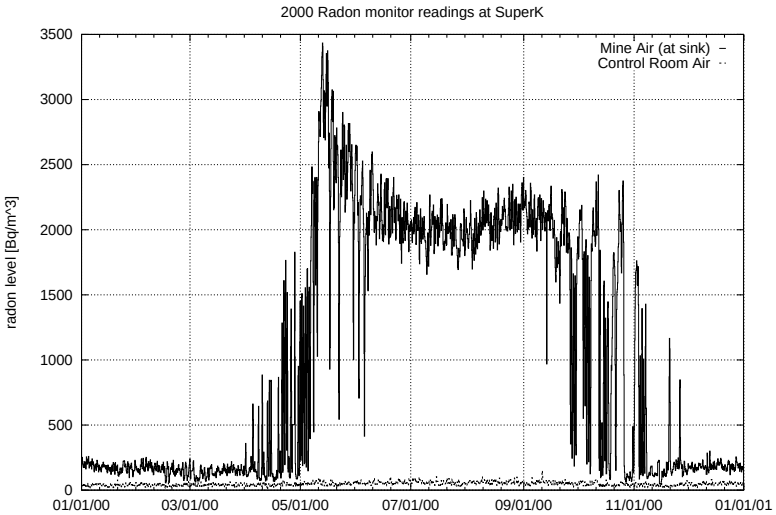

Fig. 24. Typical seasonal air radon levels at Super-Kamiokande over a year.

duct from the Atotsu entrance to the experimental area. Originally, a second air blower and air heater were also operated to regenerate the Rn-saturated carbon in the filter tanks at regular intervals, and lower the radon level of the output air down to $10\,\mathrm{Bq\,m^{-3}}$ or less. However, maintenance and expert supervision of the carbon regeneration operation turned out to be impractical for continuous running. In autumn 1997, an extended intake air pipe was installed at a location approximately 25 m above the Atotsu tunnel entrance, where radon level concentration was found to remain at 10–30 $\mathrm{Bq\,m^{-3}}$ all year long. It was decided that this low level satisfies the air quality goals and that carbon filter regeneration operations would no longer be required. As shown in Fig. 24, the $10\,\mathrm{m^3\,min^{-1}}$ fresh air flow from the radon hut keeps the radon levels in the experimental area ("Control Room Air" curve) at approximately 30–50 $\mathrm{Bq\,m^{-3}}$ throughout the year.

8. Calibrations

8.1. Water transparency measurement

8.1.1. Direct measurement with a dye laser

The optical attenuation length in water represents the combined effects of scattering and absorption on the intensity of light. It can be parameterized as follows:

$$I = I_0 \frac{1}{l^2} \exp(-l/L_{\mathrm{atten}}) \tag{3}$$

with

$$L_{\mathrm{atten}} = \frac{1}{\alpha_{\mathrm{abs}} + \alpha_{\mathrm{scat}}} \tag{4}$$

where I is the light intensity at distance l away from a source, and L_{atten} is the attenuation length.

While through-going and stopping muons, as well as other calibration studies, may be used to infer the water attenuation length, an independent direct measurement is valuable. Such measurements are done in Super-Kamiokande with a device consisting of a titanium–sapphire laser, a diffuser ball, and a CCD camera.

The tunable titanium–sapphire laser is pumped with an Nd:YAG laser, which can provide output energies of 2–3 mJ per pulse at a wavelength of 420 nm. These energies are considerably higher than those reached with the nitrogen-dye laser used initially. Using a second-harmonic generator, the attenuation length for wavelengths between 350 and 500 nm can also be measured.

To measure the attenuation length, the diffuser ball is lowered into the water and illuminated

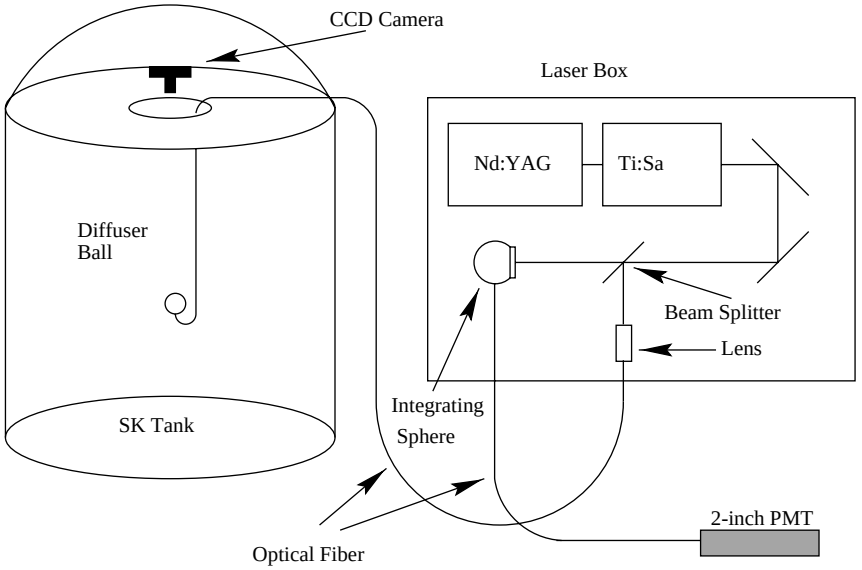

Fig. 25. Laser system for water attenuation length measurement.

with the laser via a fiber optic cable (see Fig. 25). The ball is then imaged with the CCD camera. Laser stability is monitored with a PMT. Measurements are made at various depths. For each diffuser ball position, the intensity measured by the CCD camera is normalized by the total number of ADC counts from the PMT monitor system to account for any shifts in laser intensity.

Since the water attenuation length changes with time (i.e., water quality) and wavelength, it must be measured at several wavelengths and at regular intervals. Fig. 26 is a typical attenuation curve as a function of distance from the light source for 420 nm wavelength. The attenuation length is found to be 97.9 ± 3.5 m at 420 nm as shown in Fig. 26.

Results from one such set of measurements are shown in Fig. 27 where the attenuation coefficient (L_{atten}^{-1}) is plotted as a function of the wavelength together with the prediction of the model used in the Super-Kamiokande Monte Carlo simulation (dashed-dotted lines). Here the model includes effects of Rayleigh and Mie scattering, and absorption terms. Data points marked with stars are from the light scattering measurements described in Section 8.2.

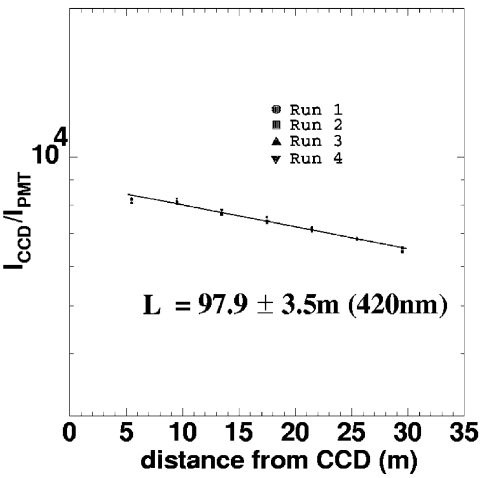

Fig. 26. Observed light attenuation as a function of the distance from the light source.

8.1.2. *Indirect measurement with cosmic rays*

The light attenuation length in water is also measured by using through-going cosmic ray muons. These muons are energetic enough to deposit almost constant ionization energy per unit path length (about $2\,\text{MeV}\,\text{cm}^{-1}$) independent of particle energy. This fact makes it possible to use these muons as a "constant" light source. The advantage of this method is that continuous and

abundant samples of muons come without cost as we take normal data. The disadvantage is that we cannot measure the transparency as a function of wavelength. However, since what we measure is the Cherenkov spectrum, this disadvantage is not necessarily a problem.

Under the assumption that light reaching the PMTs is not scattered, the charge Q observed by a PMT is expressed by

$$Q = Q_0 \frac{f(\theta)}{l} \exp\left(-\frac{l}{L}\right) \quad (5)$$

where l is the light path length, L the effective attenuation length, Q_0 a constant and $f(\theta)$ relative photosensitive area, which depends upon the incidence angle θ of the light on the PMT, as shown in Fig. 28.

Fig. 29 is $Ql/f(\theta)$ as a function of the path length l together with the best fit in the form of the function defined above. The resulting attenuation length is found to be 105.4 ± 0.5 m.

As the data sample for this measurement is accumulated automatically while we take normal data, it is possible to continuously monitor the attenuation length as a function of time. As seen in Fig. 30, the attenuation length changes with time, correlated with water quality. Such time variations are corrected by taking the attenuation length used in analysis from the time series of calibration data.

8.2. Light scattering measurement

To measure the scattering (α_{scat}) and absorption (α_{abs}) parameters separately, a combination of dye

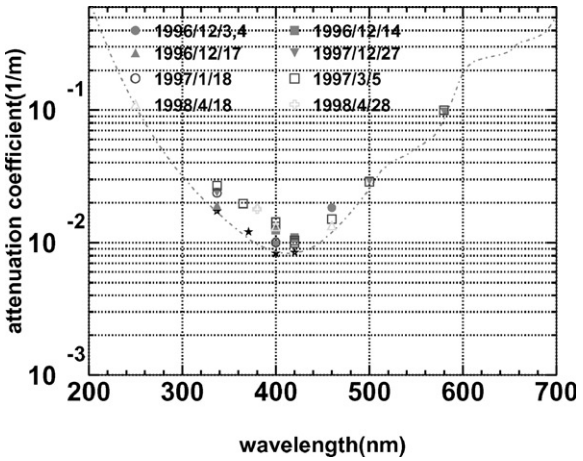

Fig. 27. Water attenuation length.

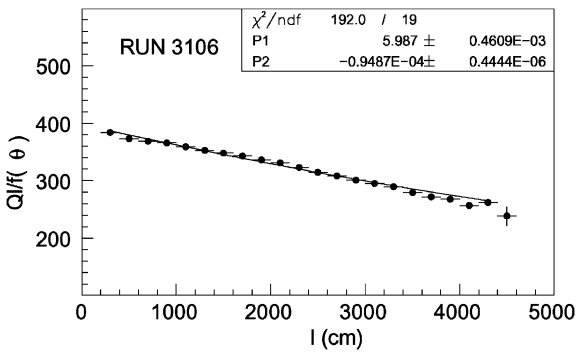

Fig. 29. Effective observed charge as a function of the path length.

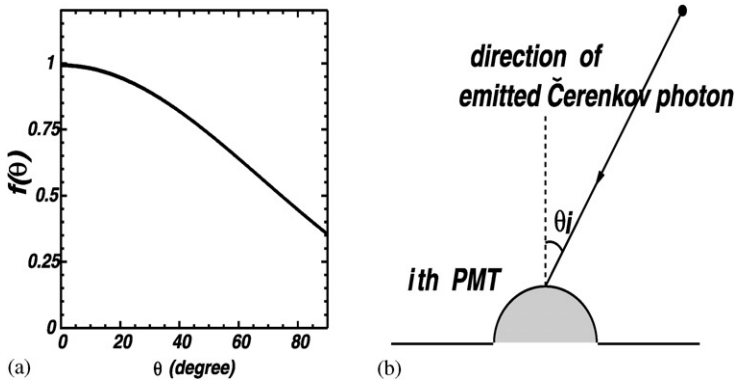

Fig. 28. Relative photosensitivity: (a) measurement result, and (b) definition of the incident angle.

and N_2 lasers of wavelengths 337, 371, 400 and 420 nm are used as light sources. The laser beam is brought into the Super-Kamiokande detector via optical fibers. Each laser fires every 6 s during normal data taking. Every 5 days, accumulated data are combined and analyzed as a single set.

Fig. 31 shows a schematic view of the laser calibration setup and a typical event using laser light. PMT hits clustered at the bottom of the tank are due to unscattered photons. The remaining hits, in barrel and top PMTs, are due to photons scattered in the water and/or reflected by the bottom PMTs.

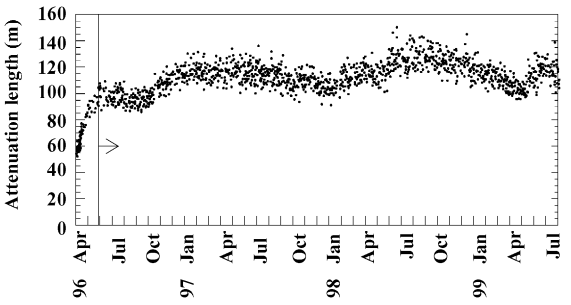

Fig. 30. Time variation of the water attenuation length.

The total charge in the cluster of bottom hits provides the light intensity reference value used for normalization. A Gaussian fit is applied to the charge distribution in the bottom PMTs, and the resulting parameters are used to adjust beam shape and direction in the calibration Monte Carlo.

Fig. 32 shows distributions of photon arrival times at the PMTs. In the upper plot, the peak near 730 ns is from scattered photons, and the second peak represents photons reflected by the bottom PMTs and black liner sheets. For the Monte Carlo, the total number of scattered photons is tuned using Rayleigh scattering parameters, and the shape of the arrival-time distribution is used to adjust the absorption parameters. The lower plot in Fig. 32 shows the time dependence of the ratio between Monte Carlo and data, which agree within $\sim 2\%$.

Using the measured absorption and scattering parameters, the light attenuation length of water is calculated using Eq. (4). Fig. 33 compares the time variation of the light attenuation length in Super-Kamiokande water as measured using the laser system and cosmic ray muons. Both independent

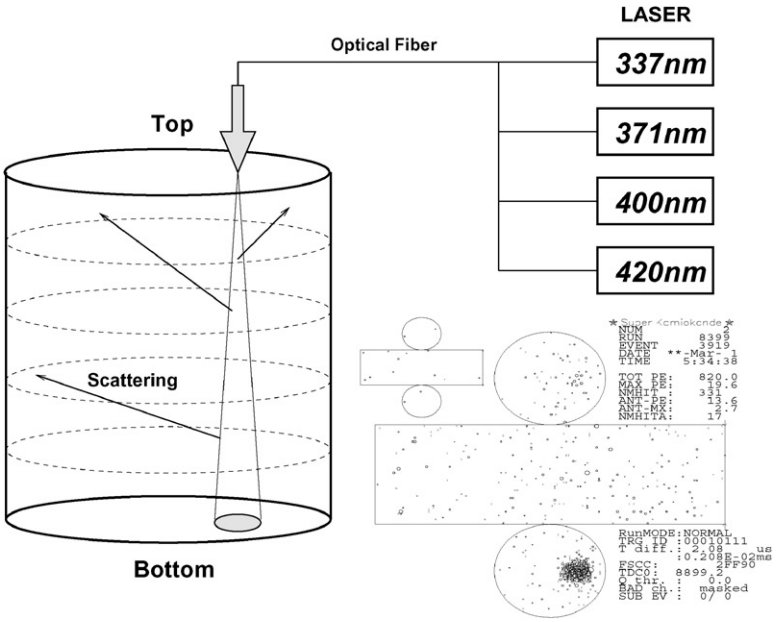

Fig. 31. Laser system for scattering and absorption parameter measurement, and a typical event.

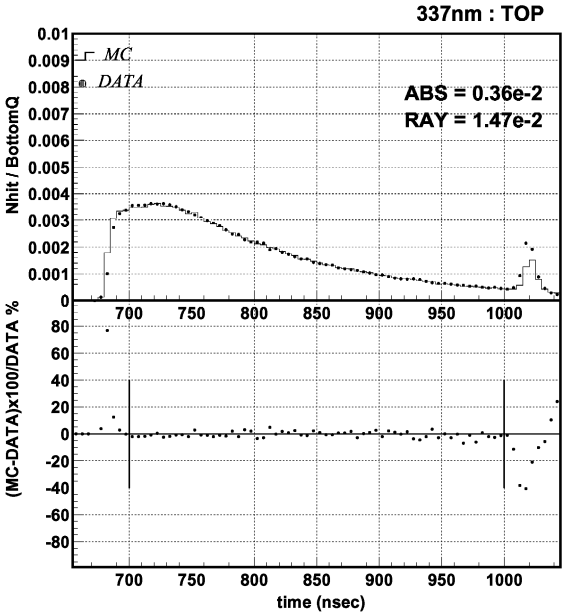

Fig. 32. The upper figure is the photon arrival-time distribution for the Monte Carlo (histogram) and data (dots). The lower figure is the ratio between MC and data as a function of time.

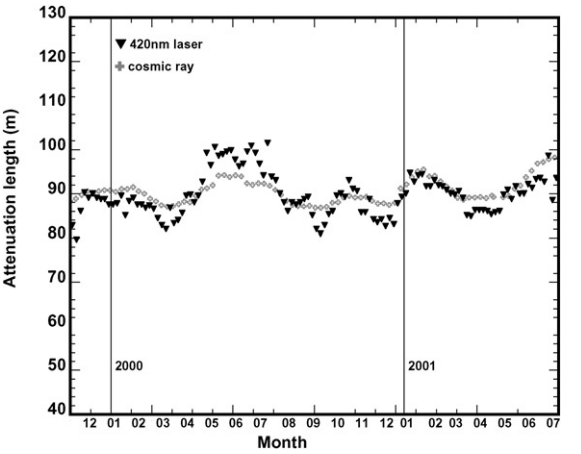

Fig. 33. Time variation of measured light attenuation length since November, 1999 using the laser system (triangles) and cosmic ray muons (crosses).

measurements show consistent variation of attenuation length.

The attenuation coefficients obtained from this method are plotted in Fig. 27 with a star symbol together with measurements with the defuser ball described in Section 8.1.2.

8.3. Relative gain calibration

The high voltage of each PMT is set to provide approximately equal gain for all PMTs in the Super-Kamiokande detector.

Each PMT came with a nominal high voltage value, which was specified by Hamamatsu Photonics just after its production, using three calibration light sources: a DC light source, a Xe-lamp pulsed light source, and a light source at the single pe level. However, because of possible long-term drift in the factory calibration system, which may have caused a systematic difference between tubes manufactured at different times, all PMTs had their gain recalibrated at the beginning of Super-Kamiokande I.

Relative gain was measured by the system shown in Fig. 34. Light generated by a Xe lamp is passed through an ultraviolet (UV) filter and injected into a scintillator ball via an optical fiber. The scintillator ball is an acrylic ball with BBOT (2,5-bis(5′-tert-butyl-2-benzoxazolyl)thiophene) wavelength shifter and MgO powder diffuser. BBOT absorbs UV light and emits light with a peak at 440 nm, which is in the sensitive region of the PMTs used for Super-Kamiokande for Cherenkov light detection. In this measurement each PMT detects a few tens of pe.

The intensity of the primary UV light is monitored by two photodiodes and one PMT. The output of the monitor PMT is also used for triggering.

The relative gain G_i of the ith PMT is obtained by

$$G_i = \frac{Q_i}{Q_0 f(\theta)} l_i \exp\left(\frac{l_i}{L}\right) \quad (6)$$

where Q_i is the observed charge by the PMT, Q_0 a constant, L the effective light attenuation length, l_i the distance from the light source to the PMT and $f(\theta)$ the relative photosensitivity as a function of the incident angle of light on the PMT defined in Fig. 28(b).

The high voltage value for each PMT is set so that the "corrected Q" of each PMT is approximately the same as for all others. Here, "corrected Q" is the pulse height corrected for

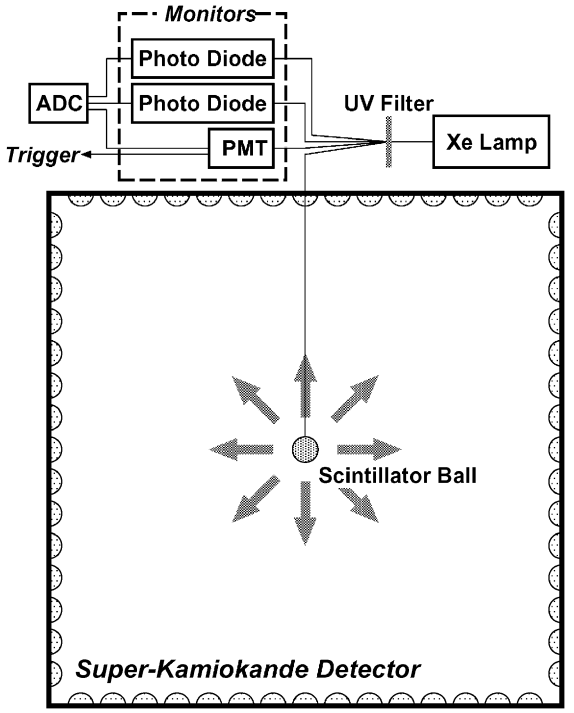

Fig. 34. The relative gain measurement system.

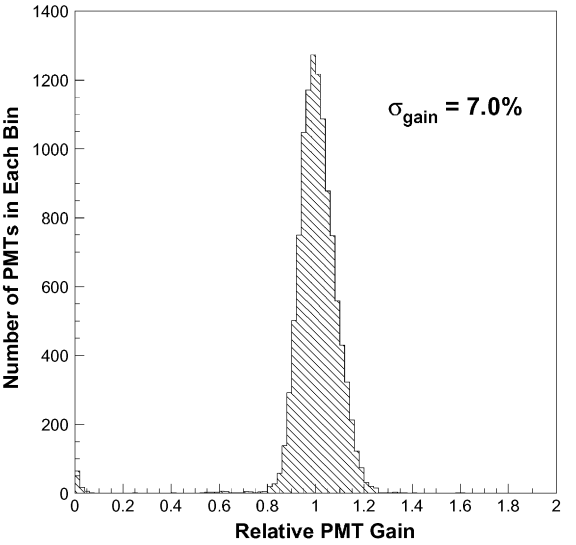

Fig. 35. The relative gain distribution measured just after recalibration and adjustment, in June, 1996.

light attenuation, acceptance of the PMT, and uniformity of the scintillator ball. It is further normalized by the Xe monitor pulse height. This measurement is done for various positions of the scintillator ball and settings of the high voltage value.

Fig. 35 shows the relative gain distribution of all PMTs after re-calibration. The horizontal axis shows the "corrected Q" normalized by its mean. The relative gain spread σ_{gain} is defined as the standard deviation obtained by fitting the distribution to a Gaussian. It was 7.0% at the beginning of Super-Kamiokande I.

After the initial gain adjustment, long term stability of PMT gain was monitored using the same system. The absolute value of PMT gain cannot be measured in situ while the experiment is running. We can only compare the variation of the gain spread σ_{gain} shown in Fig. 36. Over 28 months, between June, 1996 and September, 1998, the standard deviation of the PMT gain increased by about 10–7.7%.

8.4. Relative timing calibration

The relative timing of PMT hits is important for event reconstruction. It depends on the length of the signal cable between the PMT and the ATM, and also depends on observed charge because of the discriminator slewing effect. The timing difference in each individual PMT has to be measured precisely to get better timing resolution.

Fig. 37 shows the system for measuring the relative timing of hit PMTs. The N_2 laser can emit intense light of wavelength 337 nm within a very short time (less than 3 ns). The wavelength is converted to 384 nm, which is near the lower edge of sensitivity of a PMT to the Cherenkov light, by a dye laser module. The light intensity is changed by using an optical filter, and the PMT timing is measured at various pulse heights. After passing through the optical filter, the light goes to the diffuser ball in the detector through an optical fiber. The schematic view of the diffuser ball is also shown in Fig. 37. The diffuser tip located at the center of the ball is made from TiO_2 suspended in optical cement. The light emitted from the tip is further diffused by LUDOX® manufactured by Grace Davison, silica gel made of 20 nm glass

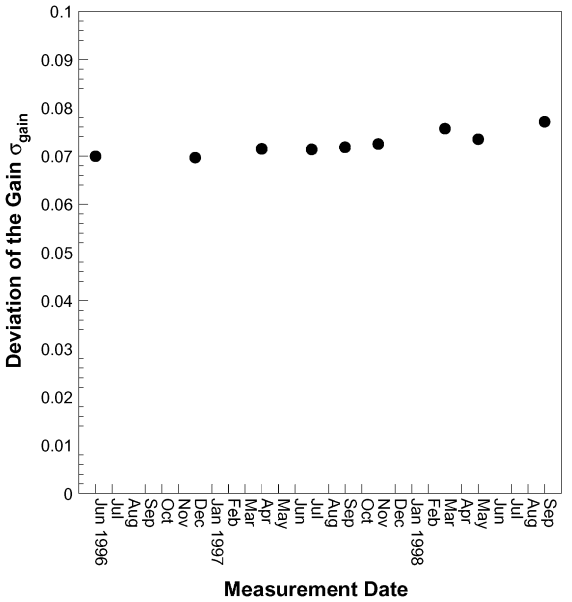

Fig. 36. The time variation of the standard deviation (over all ID PMTs) of PMT gain.

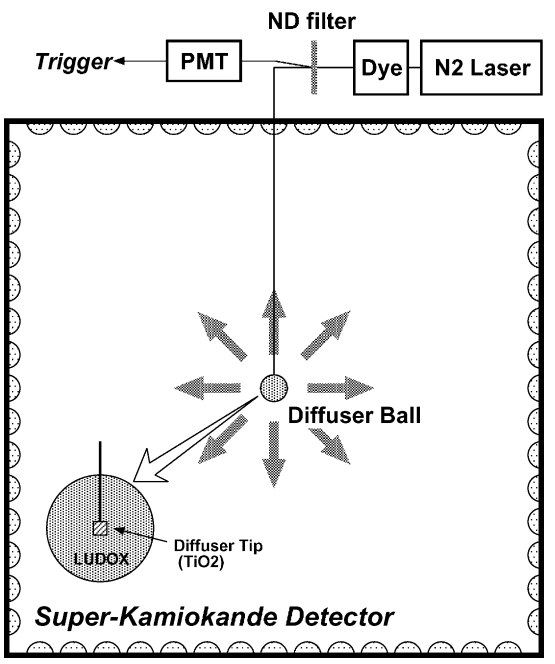

Fig. 37. The timing calibration system.

fragments. The combination of diffuser tip and LUDOX® can make modestly diffused light without introducing significant timing spread.

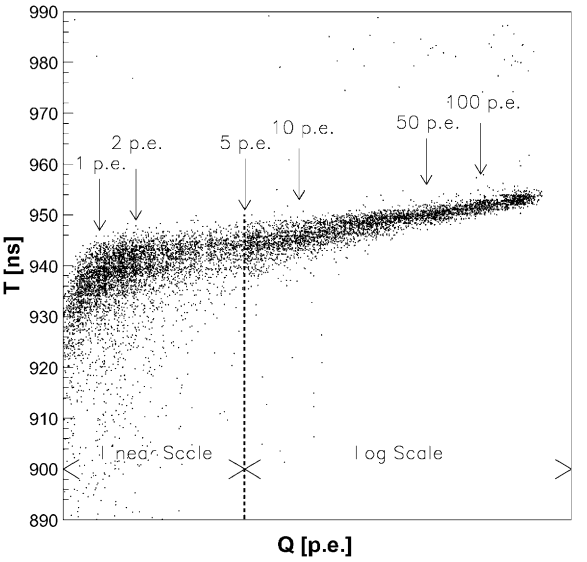

Fig. 38. A typical two-dimensional plot of timing vs pulse height distribution, referred to as a "TQ-map".

A typical scatter plot of the timing and pulse height is shown in Fig. 38, which is called a "TQ-map". Each PMT has its own TQ-map, which is applied in data reduction.

The timing resolution of PMTs as a function of pulse height is estimated from the TQ maps and is shown in Fig. 39. Typical timing resolution at the single pe level is better than 3 ns, which is important for solar neutrino analyses.

8.5. LINAC calibration

For the Super-Kamiokande solar neutrino analysis, it is essential to have precise knowledge of the absolute energy scale, energy resolution, angular resolution, spatial resolution and detection efficiency for low-energy (few MeV) electrons. For this purpose Super-Kamiokande operates an electron LINAC as a source of electrons of known energy.

Fig. 40 shows a schematic view of the LINAC system that is installed above the water tank. In this figure, the fiducial volume used for the solar neutrino analyses is indicated by dashed lines and the black dots indicate the locations where LINAC calibration data are taken.

Using the LINAC, the accuracy of the absolute energy scale is better than 1% in the energy range from 5 to 16.3 MeV. Table 5 summarizes the energy, angular and vertex resolution for electrons in the energy range 4.9–16.1 MeV.

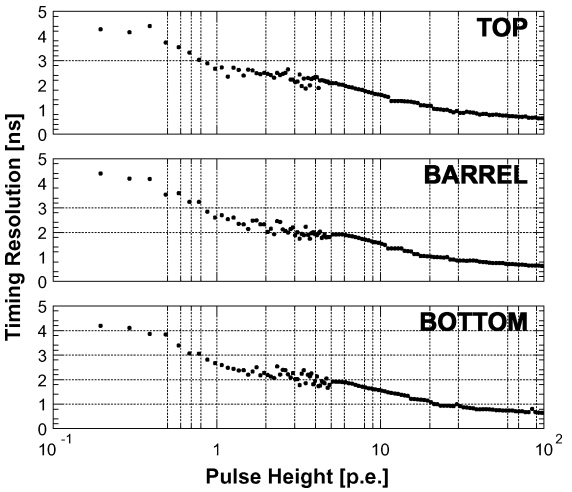

Fig. 39. Timing resolution of PMT as a function of pulse height measured in May 1998. They are the mean of 500 PMTs in each part of Super–Kamiokande.

A comparison of absolute energy scale and resolution for various parameters between the observed LINAC data and latest Monte Carlo simulation is shown in Fig. 41. The LINAC calibration data were taken once or twice per year, and good agreement, as shown in Fig. 41, was always obtained.

Details of the LINAC system and its performance can be found in Ref. [26].

8.6. ^{16}N calibration

The decay of ^{16}N provides an independent cross check on the absolute energy scale calibration for solar neutrinos obtained from the LINAC. A DTG is employed to create ^{16}N via the (n,p) reaction on ^{16}O in the water of the detector. This technique is isotropic, and has different systematic uncertainties from those of the LINAC technique.

The decay of ^{16}N, with a Q value of 10.4 MeV, is dominated by an electron with a 4.3 MeV maximum energy, coincident with a 6.1 MeV γ ray, and is well suited to check the absolute energy scale for solar neutrino measurements. With half-life of 7.13 s, ^{16}N is created in situ by lowering the DTG into the detector on a computer-controlled crane.

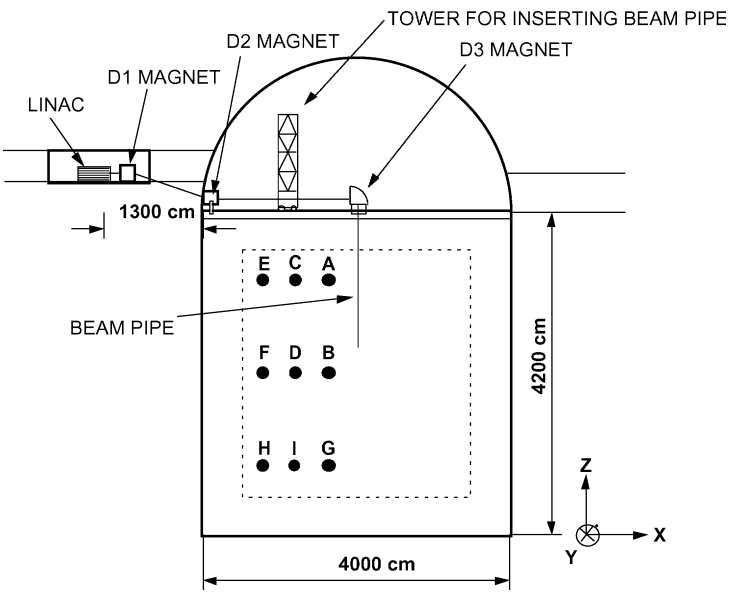

Fig. 40. LINAC system. The lettered positions indicate the locations where the end of the beam pipe is positioned in the tank for LINAC data taking.

Table 5
Experimental detector resolutions for Super-Kamiokande as derived from LINAC data

Total energy (MeV)	Energy resolution (%)	Angular resolution (degree)	Vertex resolution (cm)
4.89	20.9±0.6	36.7±0.2	182±21
5.84	19.2±0.5	34.6±0.2	133±8
6.79	18.0±0.3	32.0±0.1	108±5
8.67	16.2±0.2	28.4±0.2	85±2
10.78	14.7±0.3	25.3±0.2	73±2
13.44	13.5±0.3	22.5±0.1	65±2
16.09	12.6±0.3	20.6±0.1	50±2

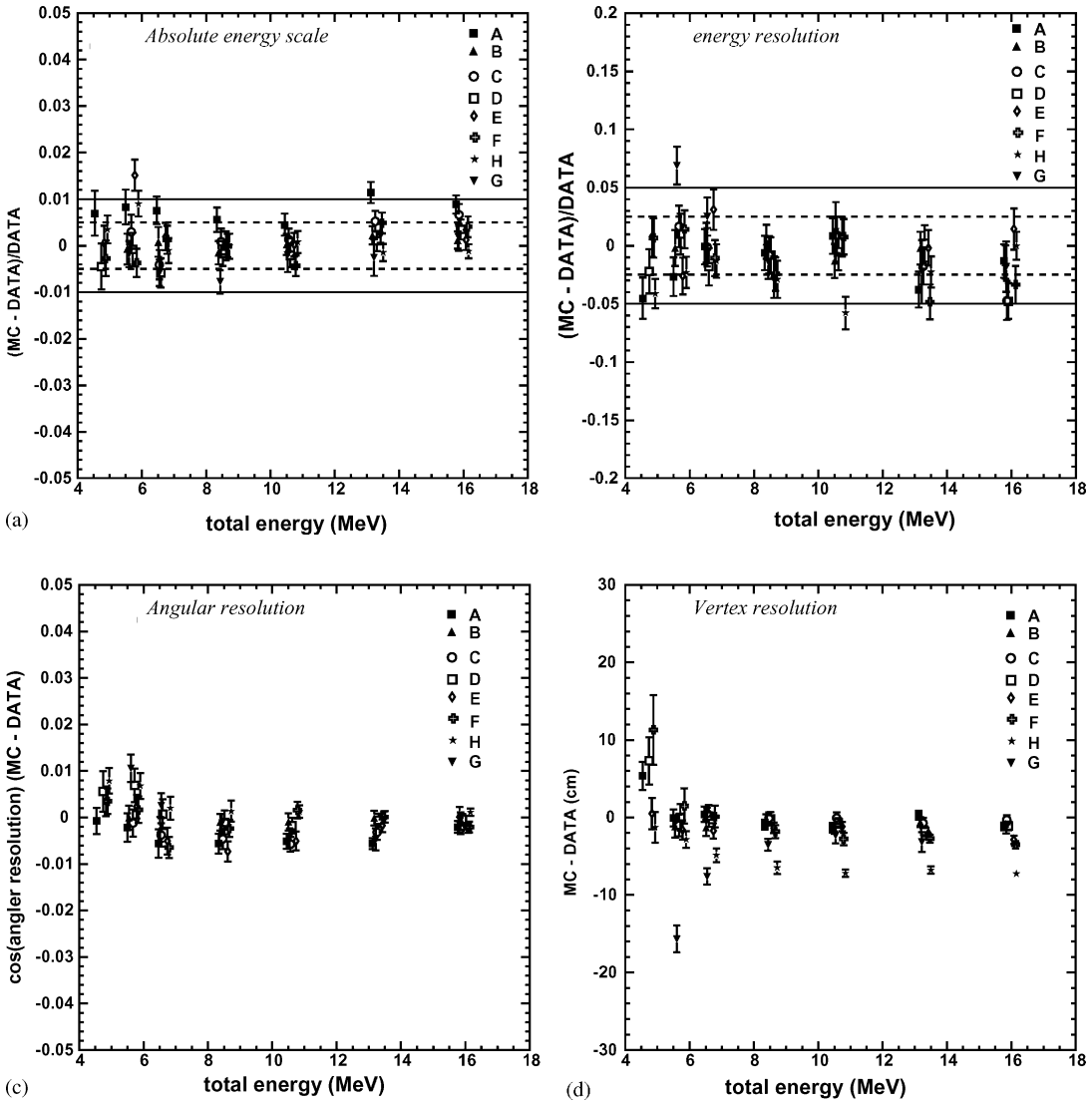

Fig. 41. Comparison of: (a) absolute energy scale, (b) energy resolution, (c) angular resolution, and (d) vertex resolution between LINAC calibration data and latest Monte Carlo simulation.

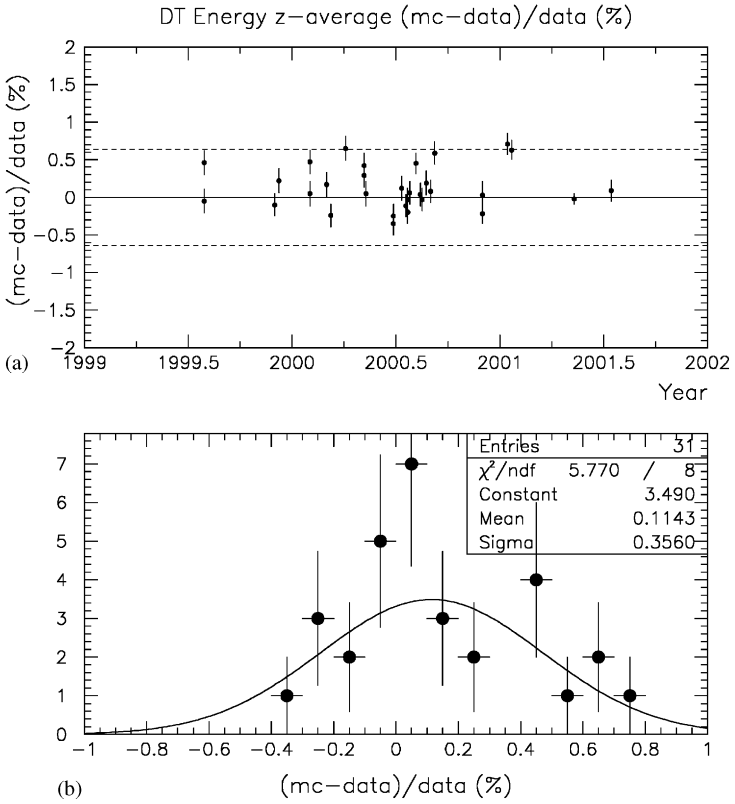

Fig. 42. (a) Agreement between the DT measurements (data) and the Monte Carlo simulation (MC) in terms of R defined in the text in percent as a function of time. Here the energy scales are averaged over z-coordinate of the source positions. (b) Distribution of R over the time period of the data used in (a).

After firing, the DTG is withdrawn, leaving the produced ^{16}N to decay unaffected by the presence of any calibration equipment. ^{16}N decays isotropically, making direction dependence studies on the energy scale possible.

Agreement between DT data and LINAC-tuned Monte Carlo is found to be within $\pm 0.64\%$ as shown in Fig. 42(a) over a long period of time where we use the ratio $R = (E_{\mathrm{Mc}} - E_{\mathrm{Data}})/E_{\mathrm{Data}}$ as a measure of the agreement. The spread in the DT measurement is consistent with a Gaussian distribution (see Fig. 42(b)).

Further details of the DTG calibration system can be found in Ref. [27].

8.7. Nickel calibration source

A Ni–Cf source was used extensively during the first two years of Super-Kamiokande operations, but was subsequently replaced by the DTG calibration source described in Section 8.6, after extensive cross-calibration. This was because of the inherent difficulty in understanding the transport of the complicated γ spectrum through the massive (1 kg) source to the required precision. Because Super-Kamiokande experience may be of value to others, we will provide some details of this calibration system.

We used thermal neutron capture on nickel as a γ source which proceeds as Ni(n,γ)Ni. Neutrons are produced by the spontaneous fission (SF) of ^{252}Cf. Approximately 97% of the time, ^{252}Cf decays via an α while the remaining 3% of the decays undergo spontaneous fission. The half-life of ^{252}Cf is 2.56 years. An average of 3.76 neutrons are produced per fission. The average neutron energy is 2.1 MeV and the spectrum extends up to about 14 MeV. The neutrons must be thermalized

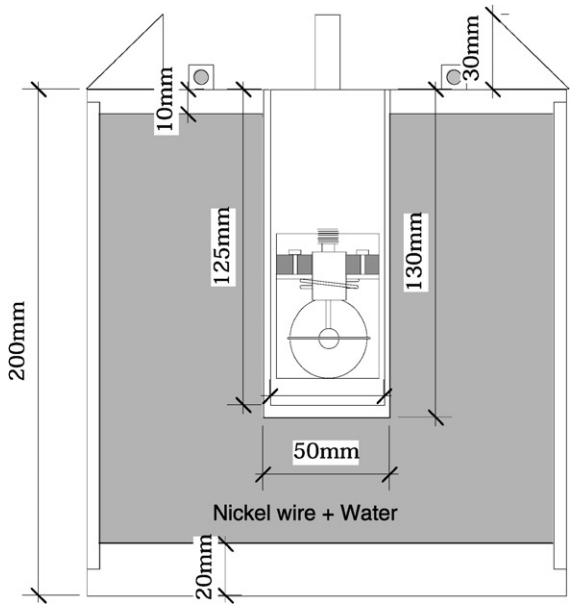

Fig. 43. Configuration of Cf-Ni *gamma*-ray calibration source. The spherical object in the middle of the source is the fission counter.

before the interaction with the nickel can proceed. The neutrons lose energy by elastic scattering off the protons in the water and it takes approximately 19 n–p scatterings (several cm of travel) and a few μs for a 2 MeV neutron to lose enough energy to be considered thermal.

Fig. 43 shows the configuration of the Ni–Cf γ calibration source. To avoid the energy dependence of trigger efficiency that distorts the spectrum and also to identify which events actually come from the source itself, an energy independent trigger called a fission trigger was used. It was implemented by using an ionization counter to detect the Cf fission products, because the events caused by the nickel source are more likely to occur soon after a fission trigger.

Since the expected life-time of fission neutrons is 83 μs, which was measured as shown in Fig. 44, background events can be distinguished from signal events using the time difference between the fission trigger and the Super-Kamiokande trigger on an event-by-event basis. Fig. 45 shows the difference in distributions of the number of hits for time differences of 10–210 μs (a) and 300−500 μs (b) between the fission trigger and Super-Kamiokande event trigger. After the background subtraction from (a) using the distribution (b), the γ signal can be extracted as (c).

Comparison of Ni–Cf source calibrations to the LINAC calibrations typically show a systematic shift of about 1.4%. Systematic errors for this source are estimated to be 2%, based on the difficulty in modeling the complicated source geometry, the shadowing of Cherenkov photons by the large container, and the complicated nuclear de-excitation process. For this reason, the Ni–Cf source is only used as a relative light source, to connect DT generator calibrations to earlier data.

8.8. Decay electrons

Decay electrons produced by stopping muons are abundant in the Super-Kamiokande data. Although these electrons do not have a monochromatic energy spectrum, we can use them to determine the absolute energy scale within a few tens of MeV.

Fig. 46 shows the momentum spectrum of the decay electrons compared with a Monte Carlo simulation that takes into account effects of the nucleon Coulomb field caused by the atomic capture of the parent muon [28]. The data distribution agrees well with the Monte Carlo prediction, and the deviation between the mean values is 2.0%.

The decay electron data are also used to monitor stability of the energy calibration, as shown in Fig. 47 where the mean values as a function of time are plotted. The mean value and absolute energy gain is stable within $\pm 1\%$ in this energy region.

8.9. Stopping muons

The Cherenkov cone angle is a function of the momentum, given by $\cos\theta = \sqrt{P^2 + m^2}/np$, where θ, p, m and n are the Cherenkov angle, momentum, mass and refractive index of the water, respectively. Using this relation and measuring the Cherenkov angle, one can calculate particle momentum. However, as the momentum increases, the Cherenkov angle quickly approaches

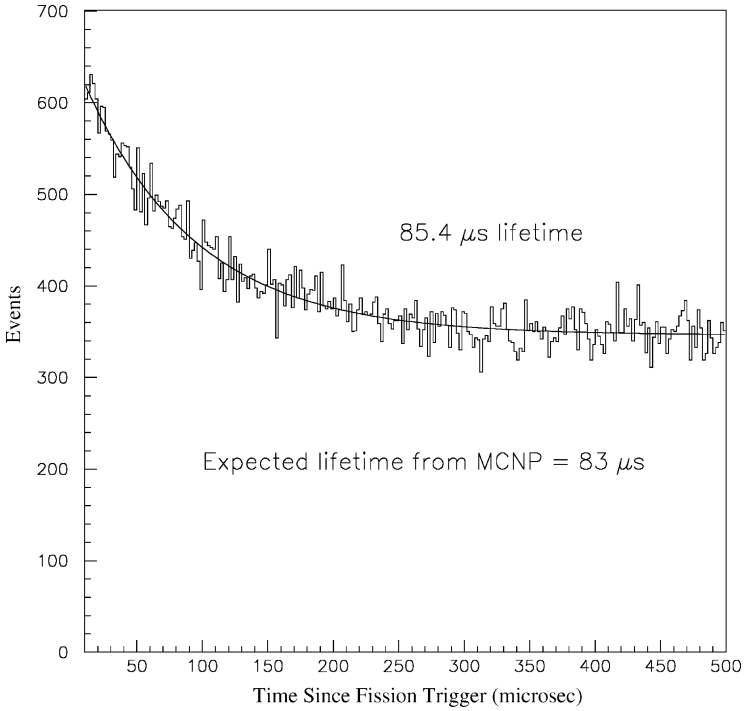

Fig. 44. Measured time between the fission trigger and low-energy event.

a limit. Therefore, this method of calculating momentum is useful only for low energy muons.

Samples of stopping muons with the momentum less than 400 MeV/c are collected to compare the measured momentum and the calculated momentum from the measure Cherenkov angle in terms of the ratio of the two quantities, R. The ratio R between the data and the Monte Carlo prediction, $R = R(\mathrm{MC})/R(\mathrm{Data})$ is plotted in Fig. 48 as a function of the momentum. In the momentum region between 0.2 and 0.4 GeV c^{-1}, R is uniform within about 1%, and is within 1.5% of the expected value (unity).

For high energy muons, the range of the muon track is proportional to the muon momentum. The range or track length is obtained by measuring the stopping point of the muon through the observed decay electron vertex position. Fig. 49 shows the ratio of momentum loss to range, for stopping muons with range greater than 7 m. The mean value for this ratio is 2.5 MeV c^{-1} cm^{-1}. Although the measured ratio is about 2.6% lower than the Monte Carlo prediction, the ratio stays almost constant within 1% over a wide momentum range.

8.10. Neutral pions

When atmospheric neutrinos interact in Super-Kamiokande via the weak neutral current, they frequently produce events with a single π^0 in the final state. These events are easily identified and can be used to check the absolute energy calibration.

After selecting events with two reconstructed rings where both are identified as showering (e-like), the invariant mass of the event is calculated assuming the rings were created by γs. The result is shown in Fig. 50. A peak from π^0's is clearly observable, at about 140 MeV c^{-2}. Both the data and MC are shifted with respect to the nominal value of the π^0 mass, 135 MeV. The shift is due to de-excitation γs from the oxygen nucleus and a 20–30 cm vertex reconstruction bias.

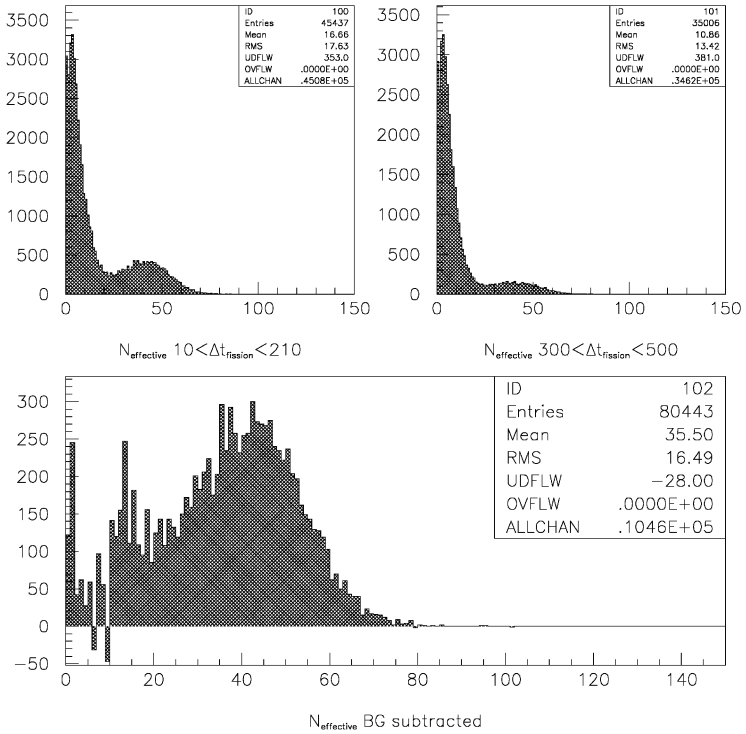

Fig. 45. N_{eff} distributions: (a) Top left: distribution with $10 \leqslant \Delta t \leqslant 210\,\mu\mathrm{s}$, (b) Top right: distribution with $300 \leqslant \Delta t \leqslant 500\,\mu\mathrm{s}$, (c) Bottom: distribution after background subtraction.

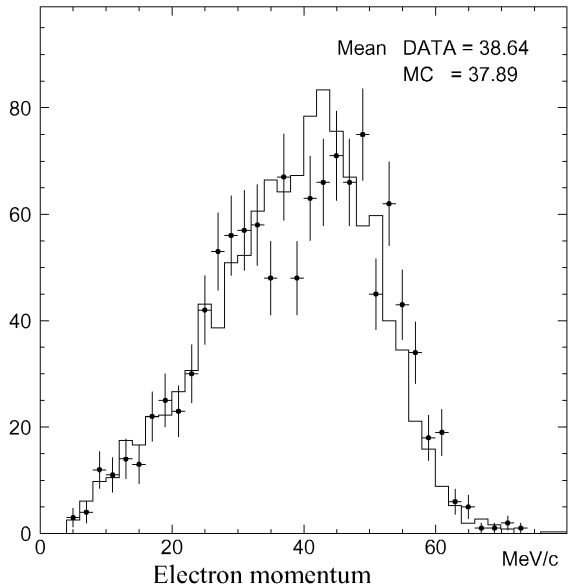

Fig. 46. The decay electron momentum spectrum from stopping muons where the histogram is the Monte Carlo prediction.

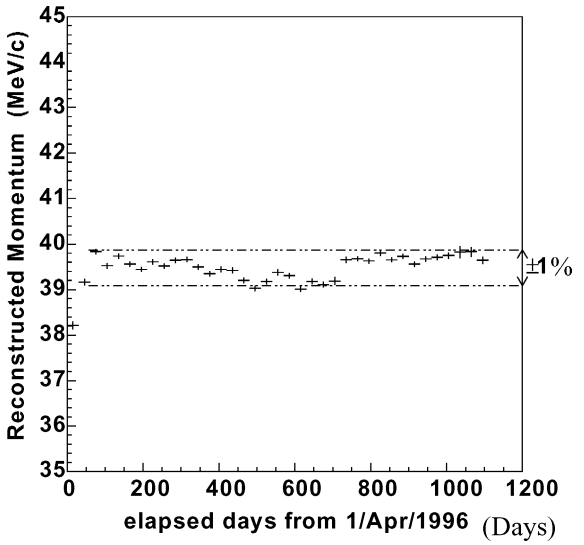

Fig. 47. The mean energy of decay electrons as a function of time.

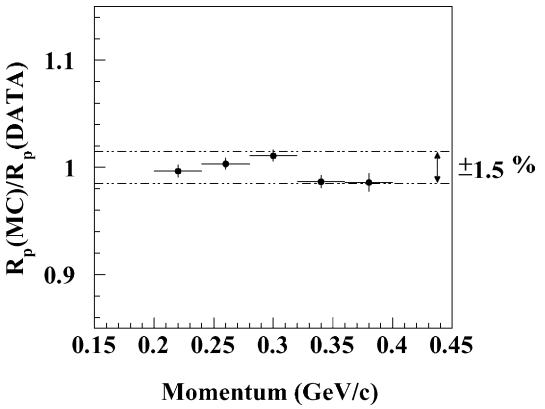

Fig. 48. Comparison of the ratio R, the measured to inferred momentum from the Cherenkov angle with the Monte Carlo prediction. The double ratio R(MC)/R(data) is plotted.

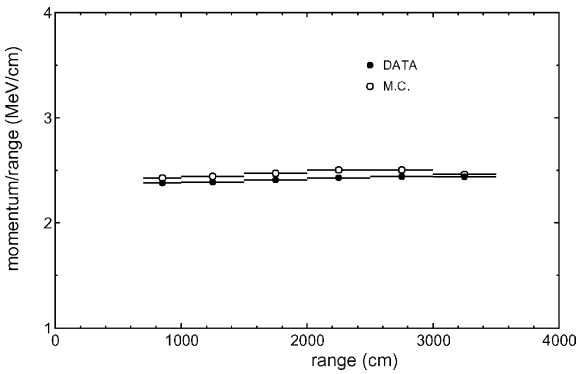

Fig. 49. The ratio the momentum loss to the range as a function of the range using high energy stopping muon samples.

Most events with a single π^0 in the final state have momenta less than 1 GeV. Efficiency for identifying single π^0's decreases with increasing momentum for two reasons. First, when a π^0 decay is highly asymmetric, one ring may be too low in energy to be reconstructed. Second, for high-momentum π^0's, symmetric decays result in small opening-angles such that the overlap of the rings is large and is not recognized by the reconstruction algorithms as two rings. Most events have a visible energy of 150–600 MeV.

The peak position of the data and MC are within 1% of each other and the widths match well, demonstrating the accuracy of the energy scale up to 600 MeV.

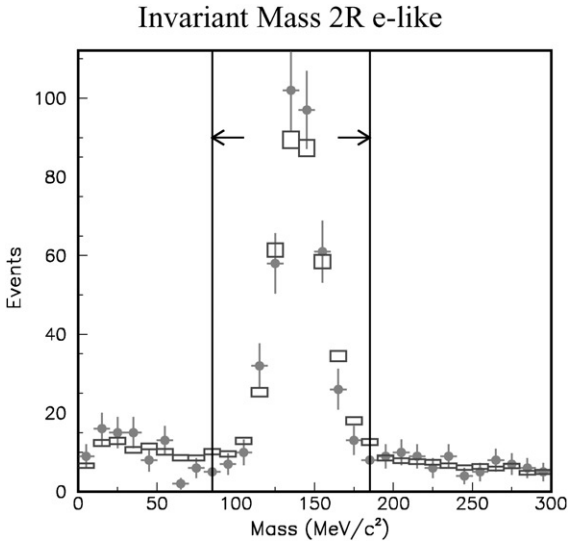

Fig. 50. The invariant mass distribution of events with 2e-like rings.

8.11. Absolute energy calibration

As described in Sections 8.5–8.9, Super-Kamiokande uses a variety of calibration methods to define the absolute energy scale over a wide energy range. Precise calibrations at low energies, using LINAC and DTG data, established a small uncertainty in the absolute energy scale (better than 1%). Fig. 51 summarizes the absolute energy scale at higher energies, in terms of agreement between the data and the Monte Carlo predictions, for the momentum range 30 MeV c^{-1}–10 GeV c^{-1}. In this energy region, the data agree with the Monte Carlo predictions within $\pm 2.6\%$.

9. Offline data processing

9.1. Offline processing at Kamioka

The offline data processing system is located at the Kenkyuto, and is connected with the online system at the Super-Kamiokande detector in the mine via a 4 km FDDI optical fiber link. After installation of a full complement of IT machines, the data flow rate from the online system is 450 kbytes s^{-1} on average, corresponding to

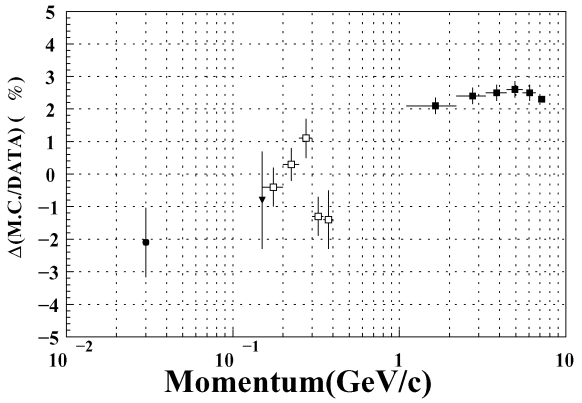

Fig. 51. Comparison of momentum measurements in the range 30 MeV/c –10 GeV/c. Solid squares represent measurements with high energy stopping muons; open squares, low energy stopping muons; solid triangles, single π^0's; solid circles, decay electrons.

40 Gbytes day^{-1} or 14 Tbytes yr^{-1}. All transmitted data are stored on magnetic tapes by the offline system, and most of the data analyses are completed there.

Because different computer architectures are expected to be used in analysis, the offline data format is designed to platform-independent. For that purpose, data structures are based on the ZEBRA bank system developed at CERN, and the ZEBRA exchange format is used. The re-formatter processes, running on Sun workstations, copy raw data files output from the DAQ event builder on the online host, and convert the data to ZEBRA format. The SLE IT filtering, using fit information copied from the IT machines, is performed in this step (see Section 5.4.2). The filtered and converted files are then sent out of the mine to be processed by the offline system.

Event data sent from the Super-Kamiokande online DAQ system basically consists of a list of hit PMT numbers, plus TDC counts and ADC counts for all hit PMTs, along with GPS time-stamps and other housekeeping data. The raw TDC and ADC count information must be converted to ns and equivalent pe for the physics analyses. However, conversion to physics quantities triples the size of the event data block. Therefore only the raw TDC and ADC counts are stored on magnetic tape, to minimize tape consumption. All data analysis programs must thus include a conversion routine when they access the raw data archive. To avoid unnecessary repetition of this CPU-intensive process, at least for initial data reduction, the individual data reduction processes which feed different analysis streams are managed in one simple data flow scheme. Raw data files are converted by a single process and written on a ram disk at the main server machine as "calibrated data". All reduction processes then read the calibrated data from the ram disk at the same time. Therefore, all reduction processes must operate as semi-realtime processes. In addition, results from these semi-realtime off-line reduction processes are fed back to the online system and used to monitor detector maintenance and operation, making stability and reliability of the offline system important for smooth detector operation.

For the solar neutrino analysis, lowering the energy threshold is a constant goal, so there is a continuous effort to improve the efficiency of reduction algorithms. Changes in calibrations or reduction methods require reprocessing of earlier data, which in turn requires large amount of CPU power and high-speed I/O access to the raw data. Typically, 10 Tbytes of raw data is processed per month.

In addition to offline reduction of experimental data, the Super-Kamiokande computer system is heavily loaded by the need for extensive Monte Carlo simulation processing.

The offline system, as configured by the end of Run I, was designed to meet the demands described above: tape storage of a large database (14 Tbytes yr^{-1}), stable semi-realtime processing, nearly continuous re-processing and Monte Carlo simulation. The computer system consists of 3 major sub-systems: the data server, the CPU farm and the network.

The data server sub-system consists of a 100-Tbyte automated Magnetic Tape Library (MTL) with a 60 CPU SMP server (30 GFLOPS) as host work station (HWS), 13 Gbytes of main memory and 1 Tbyte of RAID-5 disk system. Since the HWS is a commercial product designed as an enterprise server, it has very good fault tolerance features.

The HWS is segmented into 5 domains. One main domain has 28 CPUs, 9 Gbytes of memory and 600 Gbytes of disks. Each of the other domains has 8 CPUs, 1 Gbytes of memory and 100 Gbytes of disks. The 600 Gbyte disk of the main domain is used as a Hierarchical File System (HFS) with the 100 Tbyte MTL. The disk only stores "stub files" (pointers to a file stored in the MTL) and currently—active files. Old and unused files are automatically migrated to the MTL. Access to a stub file triggers reloading of the stored file from the MTL. Thus the HFS imitates 100 Tbytes of disk space on the 600 Gbytes of disks. Substantial bandwidth is provided between HWS and disks, and between HWS and MTL (12 Ultra SCSI for disks and 12 F/W SCSI for 12 tape drives).

The main domain has 4 AP-net network connections and 4 Fast-Ethernet connections, providing 800 Mbps (AP-net) and 400 Mbps (Fast-Ethernet) network bandwidth. The main domain also has two FDDI connections, one to the online system and the other to a WS on which all the calibrated data is copied to DLT tapes. The DLT tapes are sent to the USA for offsite analysis, and to serve as backup media stored in a different location, minimizing the risk of data loss due to fire or other disaster at Kamioka.

Each of the other domains has one AP-net and 4 Fast-Ethernet connections. Services available to normal users on the HWS are carefully limited so that the system can be protected from accidental data loss caused by user errors. For a data access to the HWS, remote-file-access tools are specially prepared for normal users. The remote-file-access tools provide better throughput than NFS and FTP protocols, and also offers convenient functions for accessing large numbers of files (for example, external file lists, file concatenation, and aliases for directory names). This limited access method makes the system safer and more stable.

The CPU farm is a simple array of $\sim$40 workstations (WS) providing $\sim$40 GFLOPS. To increase CPU performance, the WS array is much more cost effective than the SMP server and it is easy to add new machines. These WSs have the same CPU architecture as the HWS, and run the same OS. Their binary codes, therefore, are compatible with those of the HWS. The WSs are also used as user terminals and home directories are constructed on these machines. Since all kinds of jobs will run on these machines, they are less reliable than the HWS. All WSs are connected to the network sub-system via Fast-Ethernet and the I/O bandwidth is more limited. Due to limited reliability and limited network bandwidth, the CPU farm is used for Monte Carlo simulations, but not for enterprise processes or I/O consuming processes such as the semi-realtime reduction processes or data reprocessing.

The network sub-system consists of two 64-channel Fast-Ethernet switching HUBs (SW-HUB), three gigabit-Ethernets between them and AP-net torus network (among the HWS domains), and a small workstation cluster. Users are divided into three groups and each group belongs to different virtual LAN (VLAN) of a SW-HUB. Each VLAN is connected to all HWS domains and uses a different gigabit-Ethernet line. By using VLAN segmentation, traffic is distributed and bandwidth to the HWS can be increased even with slow network architecture. AP-net provides 200 Mbytes s^{-1} bandwidth per connection and is used for the data server sub-system, where huge bandwidth is required for data reprocessing.

Enterprise processes, semi-realtime processes, and reprocessing jobs are run on the HWS. Requirements of enterprise processes led to configuring the computer architecture of the HWS as a giant SMP-server.

Data flow in the semi-realtime processes and data reprocessing is as follows. The online machine copies raw data to the HFS disk of the HWS via FDDI. Each file is $\sim$40 Mbytes and corresponds to about 90 s of data after the full set of IT machines were installed. The conversion process reads raw data from the HFS disk and writes calibrated data files on a "tmpfs" buffer, which is a normal file system constructed on the main memory. Then all the specialized reduction processes access this file, requiring substantial bandwidth to the buffer. For data reprocessing, the bandwidth required is $\sim$40 Mbytes s^{-1} on average.

The memory file system provides a unique solution for the problem of serving such a large bandwidth in a stable manner. Because reduction

processes can run locally on an SMP-server, they are simple and protected from network problems. This simplicity makes the system reliable, and also encourages physicists to implement new reduction programs to pursue new analysis ideas. Arbitration can be done via the simple lock-file method. Data flow can then be controlled with a simple shell script, simplifying maintenance. Process speed can be easily improved by increasing the number of processes for a massive calculation program. This simplicity can be achieved only by a SMP-server. And massive data reprocessing can be done via an extension of the semi-realtime processes, by simply adding more and more processes. Each reduction process writes output to its own HFS disk and the traffic is distributed uniformly.

9.2. *Offline data processing in US*

At the State University of New York at Stony Brook, a system dedicated to offsite offline data processing was set up to process raw data sent from Kamioka.

Most of the reformatted raw data taken at Kamioka were copied from the host computer in the Kamioka offline computer facility, where they were stored temporarily in RAM disks, to DLT tapes mounted on a Sun SPARC 20, connected via a high speed FDDI link (later Fast-Ethernet). The DLTs were then shipped to Stony Brook where a system was set up to do offline analyses and further processing.

At Stony Brook the raw data were processed with a multi-tape DLT drive. The first stage data reduction processes were done for the high energy analysis and for the low energy analysis. The data reduction for the high energy analysis was mainly for atmospheric neutrino events and proton decay search while the low energy analysis was mainly for the solar neutrino events. The reduced data for the high energy analysis was further filtered by other reduction processes and the resulting data were stored on disks. The reduced data for the low energy were stored on DLT tapes and sent to University of California, Irvine for further processing.

The offsite offline analysis in the US continued for 3 yr until a series of detailed comparisons demonstrated that the two analysis chains (onsite and offsite) were producing equivalent physics results. After the results of the independent analyses were published, it was decided that the limited manpower available to the collaboration should be concentrated into a single combined analysis.

10. Conclusion

The Super-Kamiokande underground neutrino detector provides a unique facility for detecting neutrinos with energy greater than 4.5 MeV from a variety of sources. It was operated with extremely high net livetime efficiency, from its commissioning in early 1996 until its shutdown for upgrade in July, 2001, providing data crucial to recent progress in our understanding of neutrino oscillations. In addition to its central role in studies of atmospheric, solar, and astrophysical neutrinos, Super-Kamiokande has provided the most stringent existing limits on nucleon decay lifetimes for many channels, and serves as far detector for K2K, the world's first long baseline neutrino oscillation experiment using accelerator produced neutrino beam. In this paper, we have described details of the detector hardware, calibration procedures, online data system, and offline data reduction, as used in this operating period, referred to as Super-Kamiokande I.

Super-Kamiokande remains the world's largest underground water Cherenkov detector, with many capabilities which will not be provided by any currently approved future detector, and will continue its leading role in the future. Following the unfortunate loss of over half its photomultiplier tubes in November, 2001, rapid progress has been made in effecting repairs, and at time of writing (September, 2002), we anticipate starting Super-Kamiokande II data taking on schedule, in December, 2002.

Acknowledgements

The authors gratefully acknowledge the cooperation of the Kamioka Mining and Smelting

Company. The Super-Kamiokande detector has been built and operated from funds provided by the Japanese Ministry of Education, Culture, Sports, Science and Technology, and the US Department of Energy.

In addition, participation of individual researchers and institutions in the Super-Kamiokande detector construction and operation has been further supported by the funds from: the US National Science Foundation; the US Department of Energy OJI (Outstanding Junior Investigator) Program; the Los Alamos National Laboratory of the University of California; the Research Corporation's Cottrell College Science Award; the State University of New York at Stony Brook, Office of the Vice President of Research; the Polish KBN grant 5P03B06521; and the Korean Research Foundation (BK21) and the Korea Ministry of Science and Technology.

References

[1] Y. Fukuda, et al., Phys. Rev. Lett. 81 (1998) 1562.
[2] Y. Fukuda, et al., Phys. Rev. Lett. 81 (1998) 1158.
[3] Y. Fukuda, et al., Phys. Rev. Lett. 82 (1999) 2430.
[4] M. Shiozawa, et al., Phys. Rev. Lett. 81 (1998) 3319.
[5] Y. Hayato, et al., Phys. Rev. Lett. 83 (1999) 1529.
[6] Two reports on the Super-Kamiokande accident available at: http://www-sk.icrr.u-tokyo.ac.jp/cause-committee/index-e.html and http://nngroup.physics.sunysb.edu. The second site provides two reports while the former one report. Note that these documents are partial translation of two reports in Japanese.
[7] H. Nuomi, et al., Nucl. Instr. and Meth. A 398 (1997) 399.
[8] E.V. Bugaev, et al., Phys. Rev. D 58 (1998) 54001.
[9] W. Ootani, Master's thesis in Japanese, University of Tokyo, 1994, unpublished.
[10] Surface Optics Corp, San Diego, Report No. SOC-R950-001-0195, 1995.
[11] K. Nakamura, T. Kajita, M. Nakahata, in: M. Fukugita, A. Suzuki (Eds.), Physics and Astrophysics of Neutrino, Springer, Berlin, 1996, p. 249;
A. Suzuki, in: M. Fukugita, A. Suzuki (Eds.), Physics and Astrophysics of Neutrino, Springer, Berlin, 1996, p. 388.
[12] Becker-Szendy, et al., Nucl. Instr. and Meth. A 324 (1993) 363.
[13] A. Suzuki, et al., Nucl. Instr. and Meth. A 329 (1993) 299.
[14] KEK Data Acquisition Development Working Group, KEK Report 85–10, 1985.
[15] H. Ikeda, et al., Nucl. Instr. and Meth. A 320 (1992) 310.
[16] T. Tanimori, et al., IEEE Trans. Nucl. Sci. NS-36 (1989) 497.
[17] K.S. Hirata, et al., Phys. Rev. Lett. 58 (1987) 1490.
[18] R.M. Bionta, et al., Phys. Rev. Lett. 58 (1987) 1490.
[19] H.G. Berns, R.J. Wilkes, 11th IEEE NPSS, 1999, p. 480.
[20] K. Takahashi, M. Watanabe, K. Sato, T. Totani, hep-ph/0105204.
[21] J. Beacom, R.N. Boyd, A. Mezzacappa, Phys. Rev. D 63 (2001) 73011.
[22] A. Burrows, et al., Phys. Rev. D 45 (1992) 3362.
[23] M. Nemoto, et al., Radioisotopes 46 (1997) 710.
[24] Y. Takeuchi, et al., Nucl. Instr. and Meth. A 421 (1999) 334.
[25] Y. Takeuchi, et al., Phys. Lett. B 452 (1999) 418.
[26] M. Nakahata, et al., Nucl. Instr. and Meth. A 421 (1999) 113.
[27] E. Blaufuss, et al., Nucl. Instr. and Meth. A 458 (2001) 636.
[28] P. Hanggi, et al., Nucl. Phys. Lett. B 51 (1974) 119.